J. Fluid Mech. (2014), *vol.* 759, *pp.* 432–471.
doi:10.1017/jfm.2014.575

Time-resolved evolution of coherent structures in turbulent channels: characterization of eddies and cascades

Adrián Lozano-Durán[1,†] **and Javier Jiménez**[1]

[1]School of Aeronautics, Universidad Politécnica de Madrid, 28040 Madrid, Spain

(Received 19 March 2014; revised 16 July 2014; accepted 29 September 2014;
first published online 27 October 2014)

A novel approach to the study of the kinematics and dynamics of turbulent flows is presented. The method involves tracking in time coherent structures, and provides all of the information required to characterize eddies from birth to death. Spatially and temporally well-resolved DNSs of channel data at $Re_\tau = 930$–4200 are used to analyse the evolution of three-dimensional sweeps, ejections (Lozano-Durán *et al.*, *J. Fluid Mech.*, vol. 694, 2012, pp. 100–130) and clusters of vortices (del Álamo *et al.*, *J. Fluid Mech.*, vol. 561, 2006, pp. 329–358). The results show that most of the eddies remain small and do not last for long times, but that some become large, attach to the wall and extend across the logarithmic layer. The latter are geometrically and temporally self-similar, with lifetimes proportional to their size (or distance from the wall), and their dynamics is controlled by the mean shear near their centre of gravity. They are responsible for most of the total momentum transfer. Their origin, eventual disappearance, and history are investigated and characterized, including their advection velocity at different wall distances and the temporal evolution of their size. Reinforcing previous results, the symmetry found between sweeps and ejections supports the idea that they are not independent structures, but different manifestations of larger quasi-streamwise rollers in which they are embedded. Spatially localized direct and inverse cascades are respectively associated with the splitting and merging of individual structures, as in the models of Richardson (*Proc. R. Soc. Lond.* A, vol. 97(686), 1920, pp. 354–373) or Obukhov (*Izv. Akad. Nauk USSR, Ser. Geogr. Geofiz.*, vol. 5(4), 1941, pp. 453–466). It is found that the direct cascade predominates, but that both directions are roughly comparable. Most of the merged or split fragments have sizes of the order of a few Kolmogorov viscous units, but a substantial fraction of the growth and decay of the larger eddies is due to a self-similar inertial process in which eddies merge and split in fragments spanning a wide range of scales.

Key words: turbulence simulation, turbulent boundary layers, turbulent flows

1. Introduction

The research on coherent structures in turbulence relies on the notion that there is a set of eddies that are representative enough of the dynamics of the flow that their

† Email address for correspondence: adrian@torroja.dmt.upm.es

understanding would result in important insights into the mechanics of turbulence. In recent years, the steady increase in computer power has allowed the study of instantaneous three-dimensional coherent structures extracted from direct numerical simulations (DNSs). However, their dynamics can only be fully understood by tracking them in time. Although the temporal evolution of structures in wall-bounded flow has already been studied for small eddies at moderate Reynolds numbers (e.g. Johansson, Alfredsson & Kim 1991; Robinson 1991), a temporal analysis of the three-dimensional structures spanning from the smallest to the largest scales across the logarithmic layer, using non-marginal Reynolds numbers, had not been performed until recently (Lozano-Durán & Jiménez 2010, 2011). The present work is a continuation of those analyses. Our goal is to study the dynamics of turbulent channel flows in terms of the time-resolved evolution of coherent structures, with particular emphasis on the logarithmic layer. The results of our study will be presented in two parts, of which the present paper is only the first. In it, we describe the tracking method, define the three-dimensional eddies that are individually tracked, and characterize their temporal evolution and interactions. A subsequent paper will describe the causal relations between different kinds of eddies, and the temporal behaviour of their energy and surrounding velocity flow field.

The efforts to describe wall-bounded turbulence in terms of coherent motions date back at least to the work of Theodorsen (1952), but it was not until the experimental visualization of sublayer streaks in boundary layers by Kline *et al.* (1967), of fluid ejections by Corino & Brodkey (1969) and of large coherent structures in free-shear layers by Brown & Roshko (1974), that the structural view of turbulence gained wider acceptance. Quadrant analysis was proposed to study regions of intense tangential Reynolds stress in wall-bounded turbulent flows by Wallace, Eckelmann & Brodkey (1972) and by Willmarth & Lu (1972), and the related VITA (variable interval time-averaged) technique of Blackwelder & Kaplan (1976) was used to identify one-dimensional sections of individual structures from single-point temporal signals, and to define and characterize ejections (Bogard & Tiederman 1986). Particle-image velocimetry (PIV) experiments in the 1990s provided two-dimensional flow sections, and linked the groups of ejections to ramp-like low-momentum regions (Adrian 1991, 2005). Simultaneously, the increase in computational power and the development of new experimental techniques led to the study of full three-dimensional coherent structures (Robinson 1991). Some recent works of this type are the characterization of clusters of vortices in simulations by Moisy & Jiménez (2004), Tanahashi *et al.* (2004) and del Álamo *et al.* (2006), the generalized three-dimensional quadrant analysis in Lozano-Durán, Flores & Jiménez (2012), and the experiments of Dennis & Nickels (2011*a*,*b*) among others. However, most of these studies are restricted to instantaneous snapshots from which it is difficult to extract dynamical information.

The study of convection velocities is closely linked to that of coherent structures. Kim & Hussain (1993) extracted the streamwise propagation speed of the fluctuations of pressure and velocity in a numerical channel, and concluded that it is approximately equal to the local mean velocity, except in the near-wall region, while Krogstad, Kaspersen & Rimestad (1998) computed convection velocities in an experimental turbulent boundary layer, and found that coherent motions of the order of the boundary-layer thickness convect with the local mean velocity, but that the velocity drops significantly for the smaller scales. Interestingly, del Álamo & Jiménez (2009) found that the small scales in channels travel at approximately the local average velocity, whereas larger ones travel at a more uniform speed roughly equal to the bulk velocity. Since the bulk velocity may be larger or smaller than the local

average depending on the distance to the wall, these three results are not necessarily incompatible. The average convection velocity has also been found to depend on the flow variable or structure under consideration. For instance, ejections travel at distinctly lower speeds than sweeps (Guezennec, Piomelli & Kim 1989; Krogstad *et al.* 1998).

The first attempts to measure the lifetimes of vortices date from the experiments in grid turbulence by Cadot, Douady & Couder (1995) and Villermaux, Sixou & Gagne (1995), although with limited results. The temporal evolution of the velocity fluctuations in the logarithmic layer of turbulent channels was studied by Flores & Jimenez (2010) using minimal boxes, resulting in a scenario that is a more disorganized version of the one in the minimal simulations of the buffer layer described by Jiménez & Moin (1991). The time-resolved evolution of individual structures in a full-sized logarithmic layer was first studied by Lozano-Durán & Jiménez (2010, 2011). Those works share some features with previous studies of the dynamics of hairpin vortices, both numerical (Singer & Joslin 1994; Zhou *et al.* 1999; Suponitsky, Avital & Gaster 2005) and experimental (Acarlar & Smith 1987*a*,*b*; Haidari & Smith 1994). However, while the older works describe the evolution of individual hairpin-like vortices in a laminar flow, although in some cases with a turbulent-like profile, Lozano-Durán & Jiménez (2010, 2011) and the present paper deal with the evolution of actual eddies in fully developed turbulence.

Exploiting a different technique, Elsinga & Marusic (2010) studied the evolution of the invariants of the velocity gradient tensor (Chong, Perry & Cantwell 1990; Perry & Chong 1994; Martín *et al.* 1998) in the outer part of a turbulent boundary layer, using a dataset of time-resolved three-dimensional velocity fields obtained by tomographic PIV. They found a nearly constant orbital period of the order of tens of eddy turnovers for the conditionally averaged spiral trajectories in the invariant-parameter plane, and interpreted it as a characteristic lifetime of the energy-containing eddies. The same dataset was later used by Elsinga *et al.* (2012) to track vortices in a turbulent boundary layer, and to compute average trajectories and convection velocities. They observed non-negligible wall-normal displacements of the structures during a typical trajectory, and showed that the vortical structures and bulges are transported passively by the external velocity field without significant changes in their topology. The recent work of LeHew, Guala & McKeon (2013) also uses time-resolved PIV to examine the structure and evolution of two-dimensional swirling motions in wall-parallel planes of a turbulent boundary layer, which they take to be markers for three-dimensional vortex structures. They measure their convection velocity and lifetime, and find that the latter increases with the wall-normal distance, and that a small percentage of the vortices survive for more than five eddy-turnover times.

These observations have been used to build models for the dynamics of wall-bounded turbulence based on coherent structures. The best developed ones refer to the flow near the wall, where the local Reynolds numbers are low, and the flow is smooth enough to speak of simple objects. Examples include the papers by Jiménez & Moin (1991), Jiménez & Pinelli (1999), Schoppa & Hussain (2002) and Kawahara, Uhlmann & van Veen (2012), and the reviews by Panton (2001) and McKeon & Sreenivasan (2007). Above the buffer layer, the internal Reynolds number of the eddies is higher, the eddies are themselves turbulent objects, and their characterization is more challenging. A seminal contribution was the attached-eddy model proposed by Townsend (1961) for the logarithmic layer. Generally speaking, there are at present two different models for the dynamical implementation of the Townsend (1961) conceptual framework, both of them hitherto incomplete. The first is the

hairpin-packet paradigm, originally proposed by Adrian, Meinhart & Tomkins (2000), based on the horseshoe vortex initially described by Theodorsen (1952) and further developed by Head & Bandyopadhyay (1981), Perry & Chong (1982) and others. According to that model, several hairpin vortices are organized in coherent packets that grow from the wall into the outer region, with lifetimes much longer than their characteristic turnover times (Zhou *et al.* 1999). The growth of the packets involves several mechanisms, including self-induction, autogeneration and mergers with other packets, as discussed in Tomkins & Adrian (2003) and reviewed in Adrian (2007). The observed low-momentum regions and ejections are contained within the hairpin packet, and are reflections of the cooperative effect of the hairpins. However, the evidence for hairpin vortices far from the wall is limited, and their origin and evolution remain unclear, especially with regard to how they move away from the wall.

Other models have been proposed in which the importance of the hairpins is questioned. Pirozzoli (2011) studied the organization of vortex tubes around shear layers and concluded that the former are a by-product of the latter, most likely through a Kelvin–Helmholtz instability. In the same line, Bernard (2013) found vortex furrows to be the dominant structural entity in a transitional boundary layer and the hairpins the rotational motion created as a consequence of the furrows. Schlatter *et al.* (2014) showed that transitional hairpin vortices in fully developed turbulent boundary layers do not persist and their dominant appearance in the outer region at high Reynolds numbers is very unlikely. However, the three aforementioned works focus on the buffer layer or their vicinity and do not provide any information about the logarithmic layer and above. A more complete model has been proposed by del Álamo *et al.* (2006), Flores, Jiménez & del Álamo (2007) and Lozano-Durán *et al.* (2012), in which the flow in the logarithmic layer is explained in terms of ejections, sweeps and clusters of vortices. Reviews are found in Jiménez (2012, 2013*b*). These structures are intrinsically turbulent and complex objects, in contrast to the simpler hairpins. Ejections and sweeps are grouped into side-by-side parallel pairs, mostly one-sided rather than symmetric trios (see also Guezennec *et al.* 1989), and the predominant structure is formed by one such pair, with a vortex cluster embedded within the base of the ejection, and extending underneath the sweep. They are preferentially located in the side walls of, rather than surrounding, a low-velocity streak lodged besides a taller high-velocity structure, in a configuration that most probably corresponds to the low-momentum ramps discussed by various authors (e.g. Adrian 1991, 2005). The presence of structures with almost identical features over rough walls (Flores *et al.* 2007) and in channels without a buffer layer (Mizuno & Jiménez 2013) suggests that they are generated at all heights, or that, if they are formed at the wall, they quickly forget their origin and reach local equilibrium with the outer layers. Either way, the importance of the wall as the source of eddies is diminished, and is mostly relegated to the role of creating and maintaining the mean shear.

From the kinematic point of view (ignoring the asymmetry reported above for the ejection–sweep pairs), the hairpin packet model by Adrian *et al.* (2000) and the scenario proposed by del Álamo *et al.* (2006), Flores *et al.* (2007) and Lozano-Durán *et al.* (2012), are statistically compatible at the level of one-point velocity statistics and spectra, as shown by Perry & Chong (1982), Perry, Henbest & Chong (1986) and Nickels & Marusic (2001) for hairpin packets, and by del Álamo *et al.* (2006) for vortex clusters. Beyond that, the two models are not dynamically equivalent and, while the hairpins are seen as the cause of the low-momentum regions and of the ejections, the clusters of vortices in del Álamo *et al.* (2006) are rather considered consequences

of the streaks. The first part of this paper will be devoted to clarifying this issue by the direct observation of the temporal evolution of the different structures.

The second part of the paper is devoted to the turbulent cascade. The phenomenological explanation of the transfer of energy from large to small scales was introduced in the classical paper by Kolmogorov (1941), but the concept of a turbulent cascade in terms of interactions among eddies had been proposed earlier by Richardson (1920) and later by Obukhov (1941). In the present work, we focus on the geometrical Richardson–Obukhov model of local-in-space cascade as opposed to the Kolmogorov local-in-scale one, and occasionally refer to the momentum cascade as described by Jiménez (2012). Also, it will be shown that the most important structures have sizes above the Corrsin scale and, hence, are influenced by the injection of energy from the mean shear. As a consequence, these structures are not intended to represent the isotropic energy transfer in the sense of Kolmogorov (1941) but at most its first steps. There have been many attempts to reconcile the two different views described above, and to unravel the physical mechanism behind the cascade. In particular, it has been known for some time that the cascade is not one-directional from large to small scales, but that there is a balance between direct and inverse transfers. Most of the evidence for this backscatter originates from filtering techniques in scale space (Piomelli *et al.* 1991; Aoyama *et al.* 2005). Again, the physical details of the process remained unknown, and our goal will be to inquire whether individual structures can be observed to break or merge in ways that can be related to a cascade process.

The paper is organized as follows. Section 2 describes the numerical experiments and the method employed to identify coherent structures. The tracking method is explained in § 3. The temporal evolutions of eddies are classified according to different criteria in § 4 and their geometry analysed. Their temporal behaviour is described in § 5, their lifetimes in § 5.1, their birth, death and vertical evolution in § 5.2 and § 5.3, and the advection velocities in § 5.4. Section 6 describes the evidence for direct and inverse turbulent cascades in terms of coherent structures. Finally, a discussion and conclusions are offered in § 7. Two appendices, provided as supplementary material available at http://dx.doi.org/10.1017/jfm.2014.575, contain additional information concerning the validation of the tracking procedure and the effect of the parameters chosen.

2. Numerical experiments and identification of coherent structures

2.1. *Numerical experiments*

The parameters of the DNSs used for our analysis are summarized in table 1, and are described in more detail by Lozano-Durán & Jiménez (2014). Briefly, the code is similar to that of Kim, Moin & Moser (1987). The numerical discretization is dealiased Fourier in the two wall-parallel directions, and either Chebychev or seven-point compact finite differences in the wall-normal one. Throughout this paper, u, v and w are streamwise, wall-normal and spanwise velocity fluctuations, measured with respect to their mean, which is defined over the two homogeneous directions and time. The streamwise and spanwise coordinates are x and z, and the wall-normal coordinate, y, is zero at the wall. The only non-zero mean velocity is $U(y)$ and primed (ϕ') variables denote root-mean-squared (r.m.s.) intensities. The channel half-height is h, and '+' superscripts denote wall units defined in terms of the friction velocity u_τ and of the kinematic viscosity ν. The Kármán number is $Re_\tau = u_\tau h/\nu$. We define the global eddy-turnover time as h/u_τ, and occasionally use a local turnover

Case	Re_τ	Re_λ	L_x/h	L_z/h	Δx^+	Δz^+	Δy^+_{max}	N_x, N_z	N_y	Δt_s^+	$T_s u_\tau/h$	Symbol
M950	932	89	2π	π	11	5.7	7.6	768	385	0.8	20	○
M2000	2009	126	2π	π	12	6.1	8.9	1536	633	2.1	11	△
M4200	4164	202	2π	π	12	6.1	10.6	3072	1081	3.5	10	None

TABLE 1. Parameters of the simulations. Here Re_τ is the Kármán number. The microscale Reynolds number Re_λ is the maximum in each channel, attained in all cases near the upper edge of the logarithmic layer, $y/h \approx 0.4$. L_x and L_z are the streamwise and spanwise dimensions of the numerical box, and h is the channel half-height. We use Δx and Δz to denote the streamwise and spanwise resolutions in terms of Fourier modes before de-aliasing and Δy_{max} is the coarsest wall-normal resolution. Here N_x, N_y, N_z are the number of collocation points in the three coordinate directions, Δt_s is the average time separation between the fields stored to compute coherent structures and $T_s u_\tau/h$ is the number of global eddy turnovers used in the analysis, after transients are discarded. The symbols are used consistently in the figures, unless noted otherwise.

time y/u_τ. The Kolmogorov length and time scales are $\eta = (\nu^3/\varepsilon)^{1/4}$ and $t_\eta = (\nu/\varepsilon)^{1/2}$, respectively, where $\varepsilon(y)$ is the mean dissipation rate of the kinetic energy. We often classify results in terms of buffer, logarithmic and outer regions, arbitrarily defined as $y^+ < 100$, $100\nu/u_\tau < y < 0.2h$ and $y > 0.2h$, respectively. It was checked that varying those limits within the usual range did not significantly alter the results presented below.

The Reynolds numbers chosen, $Re_\tau = 932$, 2009 and 4164, yield scale separations of $h/10\eta \simeq 30$, 60 and 100, respectively, if we assume that the largest structures are $O(h)$ and that the smallest ones are vortices with diameters of order 10η (Jiménez *et al.* 1993; Jiménez & Wray 1998). The microscale Reynolds numbers in table 1 are computed, assuming isotropy, as $Re_\lambda = q^2\sqrt{5/(3\nu\varepsilon)}$, where $q^2 = u^2 + v^2 + w^2$, and the maximum is achieved in all cases near $y/h = 0.4$. All of the statistics are compiled over at least 10 global eddy turnovers, which will be seen in § 5.1 to be long enough with respect to the lifetimes of most coherent structures not to interference with their description.

The analysis of the temporal evolution of the flow requires storing approximately 10^4 snapshots for each simulation, implying several hundred terabytes for each channel in table 1. To keep the storage requirements under some control, the channel dimensions are kept $L_x = 2\pi h$ and $L_z = \pi h$. It was shown by Flores & Jimenez (2010) that this box size is the minimum needed to accommodate the widest flow structures, and Lozano-Durán & Jiménez (2014) showed that it results in correct one-point statistics. Structures longer than $2\pi h$ exist in larger channels (Jiménez 1998; Kim & Adrian 1999; Marusic 2001; del Álamo *et al.* 2004; Jiménez, del Álamo & Flores 2004; Guala, Hommema & Adrian 2006), and are represented in the numerics as infinitely long, but it was argued by del Álamo *et al.* (2004) and Lozano-Durán & Jiménez (2014) that their evolution times are slow enough for their interactions with the smaller scales to be represented correctly even in that case. The result is essentially healthy turbulence across the whole channel, although the behaviour of the largest structures is probably unreliable. However, spectral analysis shows that structures longer than $2\pi h$ are at least as tall as h (Hoyas & Jimenez 2006; Jiménez 2012), so that the results of our analysis should be correct for eddies approximately restricted to the logarithmic and buffer layers. In fact, no structure has been discarded from our analysis for being too large. The number of eddies constricted by the box

size is too small to influence the statistics, and the only obvious difference between our results and those in larger boxes is the 'cap' of very tall and long structures found in the size distributions in figure 5 of Lozano-Durán *et al.* (2012), which is much weaker in the equivalent distributions in figure 8(*c*,*d*) of the present paper.

2.2. *Identification of coherent structures*

In the present work, we understand by coherent structures those motions that are organized in space and persistent in time and, although some distinctions are made in the literature, we will use as synonymous coherent structures, objects and eddies.

We define structures as simply connected sets of points in which some property exceeds a given threshold, with connectivity defined in terms of the six orthogonal neighbours in the Cartesian mesh of the DNS. We study two types of structures: the vortex clusters discussed by del Álamo *et al.* (2006) as surrogates for strong dissipation and the 'quadrant' structures described by Lozano-Durán *et al.* (2012) as responsible for the momentum transfer. Both have been shown to form well-defined hierarchies in the logarithmic layer of channels, and it will be shown in § 5.1 that they retain their individuality long enough to be considered coherent.

Vortex clusters are defined in terms of the discriminant of the velocity gradient tensor, satisfying

$$D(\boldsymbol{x}) > \alpha D'(y), \tag{2.1}$$

where D is the discriminant, $D'(y)$ is its standard deviation and $\alpha = 0.02$ is a threshold obtained from a percolation analysis (Moisy & Jiménez 2004; del Álamo *et al.* 2006).

Quadrant events (Qs) are structures of particularly strong tangential Reynolds stress that generalize to three dimensions the one-dimensional quadrant analysis of Lu & Willmarth (1973). They satisfy

$$|u(\boldsymbol{x})v(\boldsymbol{x})| > Hu'(y)v'(y), \tag{2.2}$$

where $-u(\boldsymbol{x})v(\boldsymbol{x})$ is the instantaneous point-wise tangential Reynolds stress, and the hyperbolic-hole size, $H = 1.75$, is also obtained from a percolation analysis (Lozano-Durán *et al.* 2012).

Each object is circumscribed within a box aligned to the Cartesian axes, whose streamwise and spanwise sizes are denoted by Δ_x and Δ_z. The minimum and maximum distances of each object to the closest wall are y_{min} and y_{max}, and its wall-normal size is $\Delta_y = y_{max} - y_{min}$. Both types of structures are classified as being detached from the wall if $y^+_{min} > 20$, or attached to it if $y^+_{min} < 20$ (del Álamo *et al.* 2006; Lozano-Durán *et al.* 2012). Attached objects with $y^+_{max} > 100$ extend into the logarithmic layer and are denoted as tall attached. They form self-similar families with approximately constant geometric aspect ratios across the logarithmic layer, although without a clearly defined shape (Jiménez 2012). Detached objects have sizes that range from a few Kolmogorov lengths up to the integral scale. The largest ones differ little from the tall attached objects (Jiménez 2013*b*), and we will see later that they often become temporarily attached to the wall during their lives. However, most of them are small and roughly isotropically oriented, with typical sizes of the order of 15–20η in the three directions (del Álamo *et al.* 2006; Lozano-Durán *et al.* 2012), and correspond to individual Kolmogorov-scale vortices.

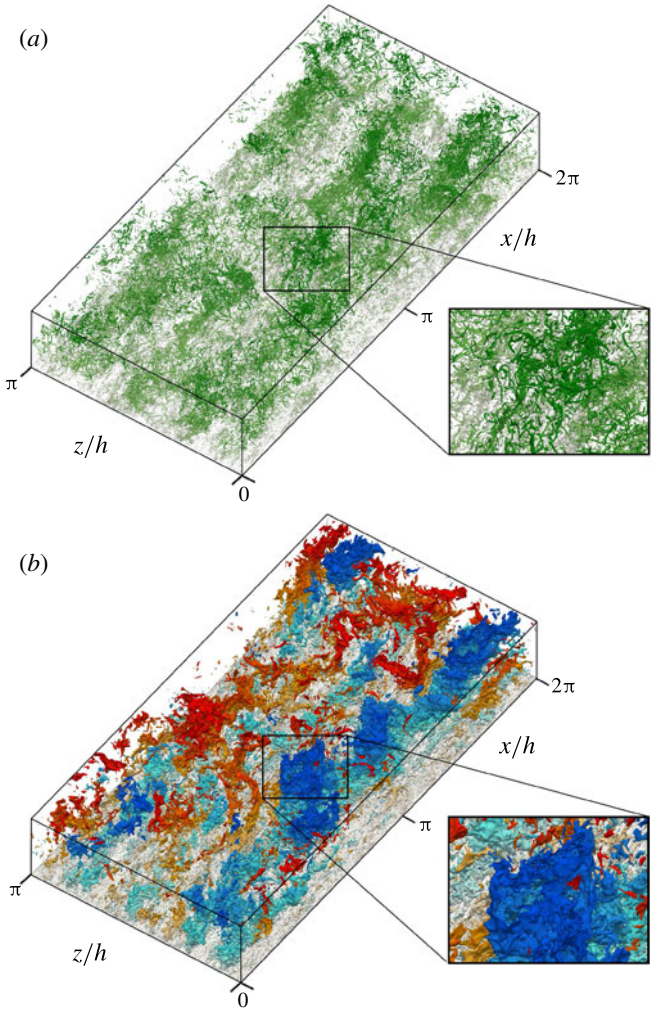

FIGURE 1. (Colour online) Coherent structures identified in a snapshot from case M4200. The structures are coloured with their distance from the wall, and only the bottom half of the channel is shown. Points close to the wall are lighter. (*a*) Vortex clusters. (*b*) Sweeps (hot colours online) and ejections (cold).

The fraction of volume contained within vortex clusters depends strongly on the threshold chosen, but is approximately 1 % of the total channel for the one used here, decreasing slowly with increasing Re_τ. Within this volume, clusters account for approximately 10–15 % of the total enstrophy, which is similar to the values found by Moisy & Jiménez (2004) in isotropic turbulence. Tall attached clusters are especially relevant because, even if we will see in § 4 that they are a relatively small fraction of the total, both by number and by volume, their bounding boxes fill a substantial part of the channel (≈20 % by volume), and intercept a correspondingly large part of the Reynolds stresses (del Álamo *et al.* 2006). They have $\Delta_x \approx 3\Delta_y$ and $\Delta_z \approx 1.5\Delta_y$, and are 'sponges of worms' whose elementary vortices have diameters of the order of 7η. Figure 1(*a*) shows all of the vortex clusters in a snapshot from case M4200, and figure 2(*a*) is a particular tall attached cluster extracted from it.

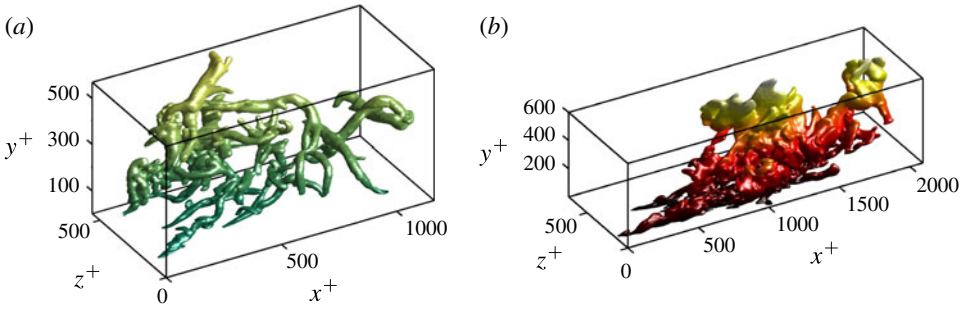

FIGURE 2. (Colour online) Instantaneous structures identified from case M4200. Both of them are attached to the wall and coloured with their distance to it. (*a*) Vortex cluster. (*b*) Sweep.

Individual Qs are classified as belonging to different quadrants according to the signs of their mean streamwise and wall-normal velocity fluctuations, computed as

$$u_m = \frac{\displaystyle\int_\Omega u(\boldsymbol{x})\,\mathrm{d}^3\boldsymbol{x}}{\displaystyle\int_\Omega \mathrm{d}^3\boldsymbol{x}}, \tag{2.3}$$

over the domain Ω of all their constituent points, where $u(\boldsymbol{x})$ is the instantaneous streamwise fluctuation velocity. A similar definition is used for v_m, $(uv)_m$, etc. As in vortex clusters, Qs of each kind separate into wall-detached and wall-attached families. The wall-attached Q$^-$s (those with $(uv)_m < 0$) are larger and carry most of the mean tangential Reynolds stress. They only fill 6 % of the volume of the channel, but are responsible for roughly 60 % of the total Reynolds stresses at all wall distances. Most wall-attached events are sweeps (Q4s, with $u_m > 0$ and $v_m < 0$) or ejections (Q2s, with $u_m < 0$ and $v_m > 0$), and form self-similar families with aspect ratios $\Delta_x \approx 3\Delta_y$ and $\Delta_z \approx \Delta_y$. They agree well with the dimensions of the uv cospectrum (Jiménez & Hoyas 2008; Lozano-Durán *et al.* 2012). Geometrically, they are 'sponges of flakes' whose individual thickness are of the order of 12η. There are very few tall attached 'countergradient' Q$^+$s, with $(uv)_m > 0$, and we will pay little attention to them. Basically, the Reynolds stress carried by the detached Q$^+$s is compensated by the detached Q$^-$s. Figure 1(*b*) shows all of the sweeps and ejections in a snapshot from case M4200, and figure 2(*b*) shows a structure extracted from it.

Table 2 summarizes some of the results described above for tall attached structures. Sweeps, ejections and vortex clusters are complex objects that are generally difficult to appreciate from a single two-dimensional view. An interactive three-dimensional view of a composite object incorporating the three kinds of structures can be downloaded from the supplementary material of Lozano-Durán *et al.* (2012), and a few more examples of individual structures can be found in our web page http://torroja.dmt.upm.es/3Deddies.

3. Tracking method

3.1. *Temporal sampling*

Since the purpose of this paper is to analyse the time evolution of individual structures, snapshots of each simulation are periodically stored every Δt_s. The sampling intervals

Structure	Sizes	Shape	Fractal dimension	Volume of the channel occupied (%)	f_c (%)
Vortex cluster	$\Delta_x \approx 3\Delta_y$ $\Delta_z \approx 1.5\Delta_y$	Sponges of worms	1.7	1	10–15
Attached Q$^-$s	$\Delta_x \approx 3\Delta_y$ $\Delta_z \approx \Delta_y$	Sponges of flakes	2.0	6	60

TABLE 2. Summary of the main features of tall attached vortex clusters and Q$^-$s. Here f_c is the fractional contribution to the enstrophy for vortex clusters or to the Reynolds stress for Q$^-$s. The fractal dimension is defined as in Lozano-Durán *et al.* (2012). See the text for details.

for the different cases are given in table 1, and were chosen to be sufficiently short to be able to track structures between consecutive snapshots. The sampling intervals in table 1 increase with Re_τ, but are always shorter than the Kolmogorov time scale, which ranges from $t_\eta^+ \approx 4$ at $y^+ = 50$ to approximately $Re_\tau^{1/2}$ in the centre of the channels. The effect of coarsening the sampling times is analysed in appendix B (see the supplementary material), but it will be shown below that the values in table 1 are short enough that only the smallest structures fail to be correctly tracked. To keep the storage requirements reasonable, only M950 was stored in full for all of the snapshots, so that the structure identification could be repeated if needed. This data set was used to tune the identification and tracking methods, and the snapshots for the other two cases only contain lists of points belonging to identified structures, although including several thresholds to study the effect of the structure intensity. In addition, about 150 complete flow fields are stored for the two higher-Reynolds-number cases, and are used to compute averages conditioned to the different structures. This procedure decreases the storage requirement by approximately 95 %, and makes the analysis in this paper possible.

Note that what is being studied here are naturally occurring structures in a fully turbulent flow, rather than tripped structures in transitional or otherwise simplified flow fields (Zhou *et al.* 1999; Wu & Moin 2010). In that sense, our results avoid some of the artifacts of simpler situations and, for example, include all of the interactions between different structures in their natural turbulent setting.

3.2. *Steps of the tracking method*

The tracking involves three stages.

(*a*) *Connections between structures*. All of the structures of a given type (i.e. either Qs or clusters) from two consecutive snapshots are copied onto a common grid, and the spatial overlaps between them are computed using the actual points of the structures. All of the structures with some overlap are considered connected (figure 3), and the operation is repeated for all of the consecutive time pairs.

(*b*) *Organization into graphs*. The result of the previous analysis is a set of backwards and forward connections between structures in consecutive frames, and needs to be processed further if the evolution of individual structures is to be studied for longer times. An object in a given frame is considered to have evolved without merging or splitting if it has exactly one backward and one forward connection. As long as that remains true, such an object can be unambiguously identified as an individual eddy. Structures with more that one

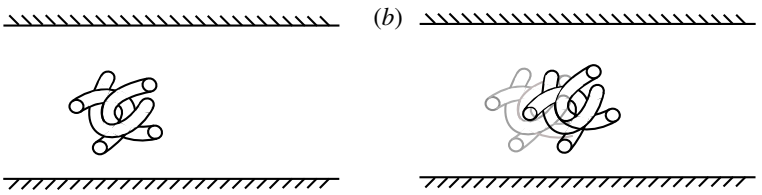

FIGURE 3. Sketch of the same coherent structure at two consecutive times. The picture corresponds to x–y views of the channel and the flow goes from left to right. The sketch in (a) shows one structure at time t_n and the picture in (b) the same structure at time t_{n+1} in dark gray, and at time t_n in light gray. The two structures overlap when copied onto a common grid and thereby a connection is created between them.

backward connection are interpreted as having merged from several pre-existing ones, and those with several forward connections are said to split (see figure 4a). A first analysis of the data shows that mergers and splits happen often enough that they cannot be ignored, and suggests the organization of the objects in a temporal graph containing all of the structures in the data set and their connections. Hence, all of the connected structures are organized into a very large graph or supergraph in which the nodes are the instantaneous structures and the edges are their temporal connections (figure 4b). This supergraph is then partitioned into singly connected components, each of which contains the evolution of all of the structures that interact with each other at some point in their lives. For simplicity, each of those individual connected subgraphs will be simply referred to as a 'graph'. Note that the organization of the structures into connected temporal graphs can be seen as a single clustering process in space–time, in which two points are assigned to the same four-dimensional cluster if they are contiguous in any of the three orthogonal spatial directions or in the forward or backwards temporal ones.

(c) *Organization into branches*. Graphs are organized into 'branches', each of which represents an individual structure. For that, each temporal connection is given a weight $\Delta V/V_i$, where ΔV is the volume difference between the structures in its two end nodes, and V_i is the volume of their overlap. Special action is only required for mergers and splits, which are defined as nodes with more than two edges. In those with more that one incoming edge, the edge with the lowest weight is defined as the primary incoming branch, while all of the others are considered parts of branches that end (merge) at that moment. Similarly, in nodes with more than one outgoing edge, the edge with the lowest weight is defined as the primary outgoing branch, and all of the others give rise to newly created branches that split at that moment. Roughly speaking, this algorithm continues as a primary branch the objects whose volume changes less across the split or merger.

A simple graph with three branches is sketched in figure 4(b), while figure 5(a) is an actual example of the temporal evolution of several vortex clusters belonging to the same graph. Figure 5(b) is the graph associated with that evolution, chosen as an example of the complex interactions that may arise. Figure 5(c) shows an actual branch classified as primary, tall attached and Q2 (see below and § 4). Table 3 shows the number of identified structures, branches and graphs for Qs and vortex clusters. Note that the numbers are in millions.

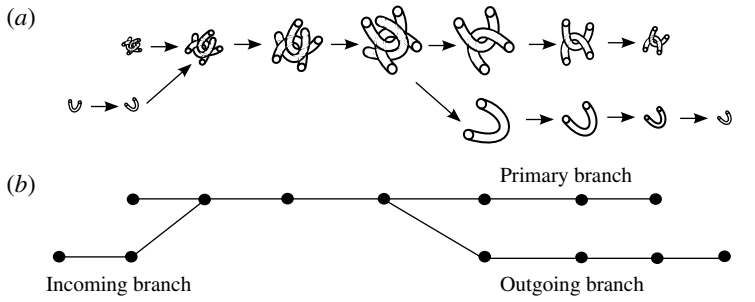

FIGURE 4. (*a*) Sketch of two structures created from the turbulent background that merge into a single one and eventually split into two fragments. (*b*) Graph associated with the evolution shown in (*a*) and its organization into branches. The graph is formed by three branches. The primary branch is continued throughout the largest object and new secondary branches are created for the fragments split and merged.

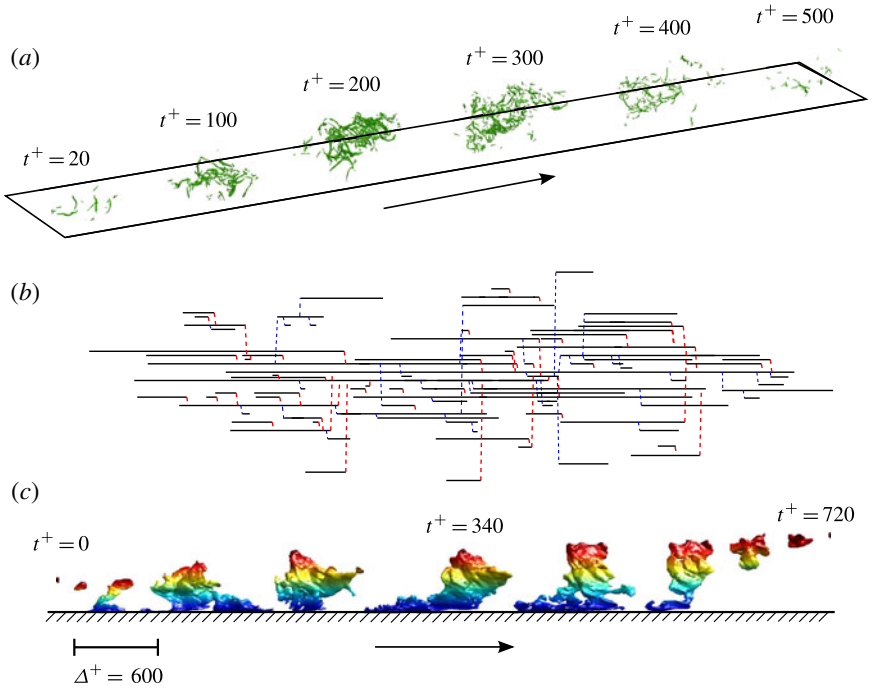

FIGURE 5. (Colour online) (*a*) Example of the temporal evolution of several vortex clusters belonging to the same graph for case M4200. The time goes from left to right. (*b*) The associated graph. The horizontal solid lines are branches, and the vertical dashed ones, mergers (red online) or splits (blue online). (*c*) Example of a primary branch extracted from case M4200 and classified as a tall attached ejection. The flow (and time) goes from left to right and the streamwise displacement of the structure has been shortened in order to fit several stages of its lifetime in less space. The structure is coloured with the distance from the wall. Note the different behaviours of its upper and near-wall components.

The tracking procedure in step (*a*) does not always succeed, especially for very small structures. The main reason is that a structure may be advected between snapshots by a distance larger than its length. To partly compensate for advection,

Case	Clusters				Qs			
	Objects	Branches	Primaries	Graphs	Objects	Branches	Primaries	Graphs
M950	185.7	6.6	2.8	1.9	107.8	3.2	1.3	1.8
M2000	397.8	19.4	8.8	6.2	294.7	18.6	11.0	9.4
M4200	799.2	45.8	19.7	36.9	889.5	64.1	35.3	32.6

TABLE 3. Number of identified structures, branches, primary branches, and graphs. All numbers are in millions.

which is mostly due to the mean flow (Taylor 1938; Kim & Hussain 1993; Krogstad *et al.* 1998; Jiménez 2013*a*), the structures at time t_{n+1} are shifted (and, hence, deformed) by $-U(y)\Delta t_s$ in the streamwise direction before their connections are computed during the tracking. Even if this procedure allows us to track smaller structures than would be possible otherwise, only those with lifetimes longer than Δt_s can be captured, and structures much smaller that $U(y)\Delta t_s$ may be occasionally lost. For that reason, objects with sizes of the order of a few wall units may look artificially isolated in time from the point of view of our method. Appendix A (see the supplementary material) presents more details and several validation tests for the tracking procedure, including for the shifting step just described, but some idea of how many connections are being missed can be gained from the number of structures that remain isolated after the tracking step, without any temporal connection. They typically represent less than 1 % of the total number of structures, and are small objects. In the case of clusters, where we have seen that the statistics are dominated by the small-scale end of the size distribution, the average volume of the isolated structures is 10–20 % of the average volume computed for all of the clusters. In the case of the Qs, the volume of the isolated objects is even smaller, approximately 1 % of the average.

3.3. *Classification of branches according to their endpoints*

Branches can be further classified according to how they are created and destroyed. Sketches for the different cases are depicted in figure 6(*a–d*). When a branch is born from the turbulent background (i.e. its first node has no backwards connections) and ends in the same way (its last node has no forward connections), it is classified as 'primary' (figure 6*a*). Secondary branches may be 'incoming', if they are born from scratch and end in a merger (figure 6*b*), 'outgoing' if they are born from a split and end into the background (figure 6*c*), and 'connectors' if they go from a split to a merger (figure 6*d*). Primary branches can be considered to represent the full lives of individual structures, and will be our main interest in the following analysis. Their number for the different cases have been incorporated into table 3. For Qs in M4200, primaries represent 52 % of all branches, incoming branches represent 20 %, outgoing ones 27 % and connectors 1 %. For the vortex clusters, primaries are 43 %, incomings are 16 %, outgoings are 39 % and connectors are 2 %. The results for M950 and M2000 are qualitatively similar. Note that the unbalance between the number of incoming and outgoing branches can be interpreted as a measure of the predominance of the direct cascade towards smaller structures over the inverse one towards larger ones. This point will be addressed in more detail in § 6.

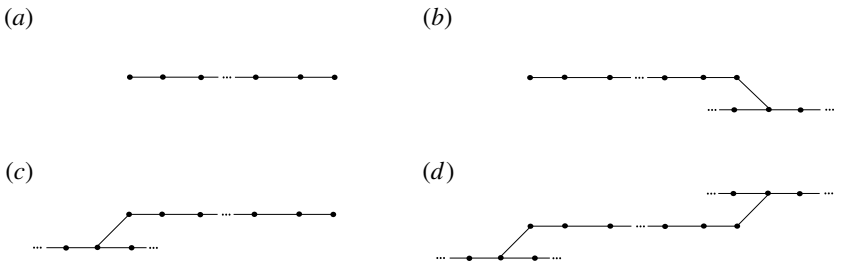

FIGURE 6. Classification of the branches attending to their beginning and end: (*a*) primary; (*b*) incoming; (*c*) outgoing; (*d*) connectors.

4. Classification and geometry of branches

Graphs and branches can be classified in much the same way as instantaneous structures. For example, we saw in § 2.2 that the structures that are attached to the wall and tall enough to reach the logarithmic layer play an important role in the dynamics of the flow. Branches are intended to represent the temporal evolution of individual structures but, since eddies cannot be expected to remain attached or detached during their whole evolution, we will classify a branch as attached if its structure is attached to the wall at some point in its life. Similarly, a branch is classified as tall attached if it contains at least a tall attached structure ($y^+_{max} \geqslant 100$); detached branches are never attached to the wall; and buffer-layer ones spend all of their lives within the buffer layer ($y^+_{max} < 100$). The same nomenclature applies to graphs, even if each graph represents the evolution of a more complex group of related structures.

Branches of Qs are assigned quadrants in the same way as individual structures. It was shown in Lozano-Durán *et al.* (2012) that all of the points within a given Q-structure belong to the same quadrant, essentially because moving from one quadrant to another involves a discontinuous change in the velocity fluctuations that is unlikely to occur between neighbouring points in a spatially well-resolved flow field. In the same way, a discontinuous change in the quadrant of a structure is unlikely to happen in a temporally resolved simulation, and branches and graphs retain their quadrant classification over their evolution. In fact, no discontinuous change of quadrant was found in any of the branches of our data base, even if no effort was made in the tracking step to connect Qs with structures of the same quadrant.

To continue our study of branches we define their geometrical properties as temporal averages over their constituent structures. Thus, the length l_x of a branch is taken to be the temporal average over the branch lifetime, $\langle \Delta_x \rangle_B$, of the length of the single structure it tracks, and the same is true of its height l_y and width l_z. A similar definition is used for the volume V_b of a branch, which is the temporal mean of the volume of its constituent structure, and the height of its centre of gravity, which is the temporal mean, y_c, of the instantaneous centres, $Y_c = (y_{min} + y_{max})/2$.

Table 4 summarizes the fractional contribution of each kind of branch with respect to all of the branches of its same type (i.e. Qs or clusters), expressed both in terms of number of branches and of total volume. It is seen that most branches are small, either detached or confined to the buffer layer, which is also true for individual structures (del Álamo *et al.* 2006; Lozano-Durán *et al.* 2012). On the other hand, the distribution of the volumes is different for clusters than for Qs. While 76 % of the volume of the Q-branches is concentrated in tall attached sweeps and ejections,

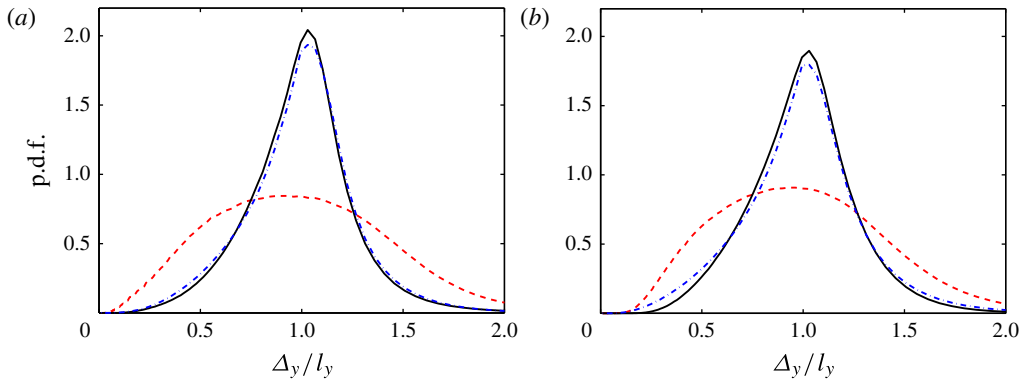

FIGURE 7. (Colour online) Probability density function of the height of the structures in primary branches, Δ_y, normalized with the mean height of their branch, l_y: ——, detached; – – – –, buffer layer; - - - -, tall attached. Case M4200. (*a*) Q^-s. (*b*) Vortex clusters.

	By number				By volume			
	Q2	Q4	Q^+	Clusters	Q2	Q4	Q^+	Clusters
Buffer layer	**0.167**	**0.161**	**0.177**	**0.509**	0.023	0.026	0.055	**0.323**
Detached	**0.169**	**0.148**	**0.175**	**0.471**	0.034	0.050	0.053	**0.490**
Tall attached	0.002	0.001	0.000	0.021	**0.476**	**0.284**	0.016	0.188

TABLE 4. Fractional contribution of different types of branches, expressed both by number and by volume. All the entries for clusters and for Qs sum to unity independently. The most important contributions are highlighted in bold. Case M4200.

even if they represent less than 1 % of the total number, 81 % of the volume of clusters is in relatively small detached or buffer-layer branches. This distribution is consistent with the different spectra of the two quantities. While the small-scale vorticity is dominated by Kolmogorov-scale vortices, momentum transfer is associated with large-scale features of the order of the integral scale. Although compiled for a single Reynolds number, table 4 is representative of the results for our three cases.

Average values taken over branches are relatively good representations of the instantaneous structures. We will see below that the lifetime of a structure is roughly proportional to its size, so that the most abundant small Qs and vortex clusters also have relatively short lives. They emerge momentarily above the thresholding intensity, and their properties change little before they disappear again. This is shown in figure 7 by the probability density functions (p.d.f.s) of the heights of the individual structures in a primary branch, normalized by the mean branch height. Both for Qs and for clusters, the p.d.f.s for detached or buffer-layer branches are concentrated around unity, and only those of the larger tall attached branches show a wider spread. The easiest interpretation is that even large branches are necessarily created and destroyed as small structures, and that their longer lives gives them the opportunity to scan a wider range of sizes. There is relatively little skewness of the distributions towards smaller or larger sizes, suggesting a relatively smooth size variation. This is confirmed by the temporal evolution of the p.d.f.s of the dimensions of the structures (not shown), which reveals that their lives are approximately evenly divided into

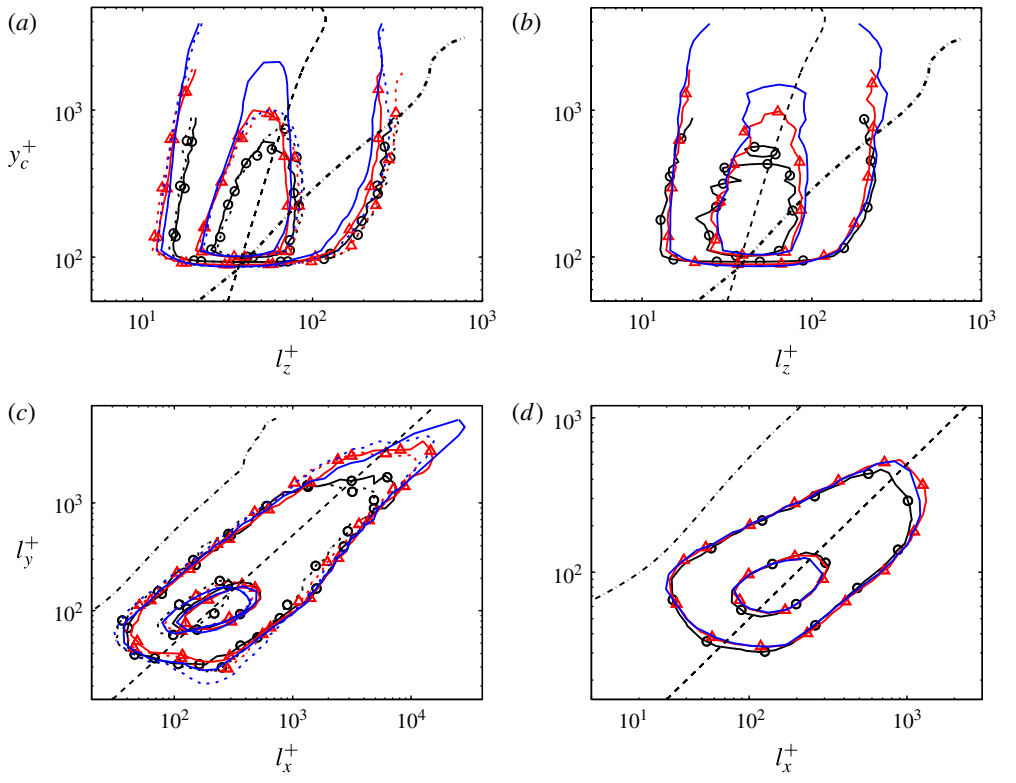

FIGURE 8. (Colour online) Joint probability density functions of the logarithm of the streamwise or spanwise average length of branches. Contours enclose 50 and 98 % of the data. (*a*) Spanwise width of detached primary Q$^-$s, as a function of the wall-normal distance of their centre of gravity, y_c. The dashed diagonal is $l_z = 15\eta(y_c)$. ——, Ejections; - - - -, sweeps. (*b*) As in (*a*), for detached vortex clusters. (*c*) Streamwise length of tall attached primary Q$^-$s, as a function of their wall-normal size, l_y. The dashed diagonal is $l_x = 2l_y$. ——, Ejections; - - - -, sweeps. (*d*) As in (*c*), for tall attached clusters. The dashed-dotted line in all of the figures is the Corrsin scale $l_c(y) = (\varepsilon/S^3)^{1/2}$ with $y = l_y/2$ or $y = y_c$, and $S = \partial_y U$. Symbols as in table 1.

a relatively uniform initial growth, an intermediate constant phase and an equally smooth final decay.

Figure 8(*a*,*b*) show the joint p.d.f.s of the spanwise size of the detached primary branches and the height of their centre of gravity, y_c. As mentioned in § 2.2, most detached structures are small objects of the order of the Kolmogorov scale, and it is significant that the average size of the branches follows the same trend, $l_z \approx 15\eta$, mentioned in § 2.2 for individual objects. This agrees with the narrow p.d.f.s for the detached branches in figure 7.

The joint p.d.f.s of the sizes of the tall attached primaries are given in figure 8(*c*,*d*). Both the Q$^-$s and the vortex clusters follow self-similar aspect ratios

$$l_x \approx 2l_y \quad \text{and} \quad l_z \approx l_y, \tag{4.1}$$

although the latter is not shown in the figure. The streamwise aspect ratio is somewhat lower than for individual tall structures, in which $\Delta_x \approx 3\Delta_y$ (del Álamo *et al.* 2006;

Lozano-Durán *et al.* 2012). That difference is consistent with the evidence in figure 7 that tall branches contain many smaller structures that bias their aspect ratio towards isotropy. Since even large structures are roughly isotropic in the cross-stream plane, $\Delta_z \approx \Delta_y$ (del Álamo *et al.* 2006; Lozano-Durán *et al.* 2012), their spanwise aspect ratio is maintained by the branches.

Note that the self-similarity of vortex clusters is less clear-cut than for the Qs. In particular, while the maximum size of the Q^- primaries scales in outer units, and keeps growing with the Reynolds number when scaled in wall units, the vortex clusters do not go beyond $l_y^+ \approx 700$. This was already noted by del Álamo *et al.* (2006) and Lozano-Durán *et al.* (2012), who remarked that, although vortex clusters tend to be associated with Q2s, they also tend to be restricted to their near-wall roots.

In the buffer layer (not shown), most of the branches are small, with sizes of the order of the well-known quasi-streamwise vortices in that region, $l_x^+ \approx 150$ and $l_z^+ \approx 80$ (Kim *et al.* 1987; Robinson 1991).

The four panels of figure 8 include the length $l_c = (\varepsilon/S^3)^{1/2}$, where $S = \partial_y U$, which was introduced by Corrsin (1958) as the size limit below which structures should not feel the effect of shear and remain essentially isotropic. This was shown to be the case for the E_{uv} cospectrum by Saddoughi & Veeravali (1994) in a high-Reynolds-number boundary layer, and for the velocity and vorticity isotropy tensors in several shear flows by Jiménez (2013*b*). Figure 8 is probably the first time that the effect is documented for individual structures. Small detached branches are approximately isotropic because they have sizes of the order of, or below, the Corrsin scale, while tall attached ones are elongated in the streamwise direction because they are larger than l_c.

5. Temporal evolution

5.1. *Lifetimes*

The lifetime, T, of a structure is the time elapsed between its first and last appearance in a branch, but that definition is only unambiguous for graphs or for primary branches. Secondary branches begin or end in splits or mergers, and it is unclear whether their lifetimes should be continued into the branch from where they split or into which they merge. In this section we will mostly concern ourselves with primary branches. Figure 9(*a*) shows the relation between lifetimes and sizes of detached primary sweeps and ejections, which scale well with the Kolmogorov times at the height of their centres of gravity, $T = 5t_\eta(y_c)$. This supports the interpretation that they are essentially viscous structures with short lifetimes, although it is interesting that there is, at all heights, a tail of longer lives suggesting enhanced coherence. It was already noted by Jiménez (2013*b*) that there is a continuous transition between large detached objects and coherent attached ones. Although figure 9(*a*) refers only to Q^-s, no significant differences are found between the lifetimes of detached Qs of any kind, or of vortex clusters.

The Q^-s in the buffer layer have lifetimes of $T^+ \approx 30$ (not shown), with extreme cases in which $T^+ \approx 400$, comparable with the bursting period of the buffer layer (Jiménez *et al.* 2005), and with the vortex decay times in that region, $T^+ \approx 200$ (Jiménez & Moin 1991; Jiménez & Pinelli 1999). The lifetime distributions for buffer-layer clusters have similar tails, but many of them live very little, near the temporal resolution limit of the present simulations.

Figure 9(*b*) shows that the lives of the tall attached Q^-s are proportional to the local eddy-turnover time, $Tu_\tau/l_y \approx 1$. This makes those branches self-similar not only

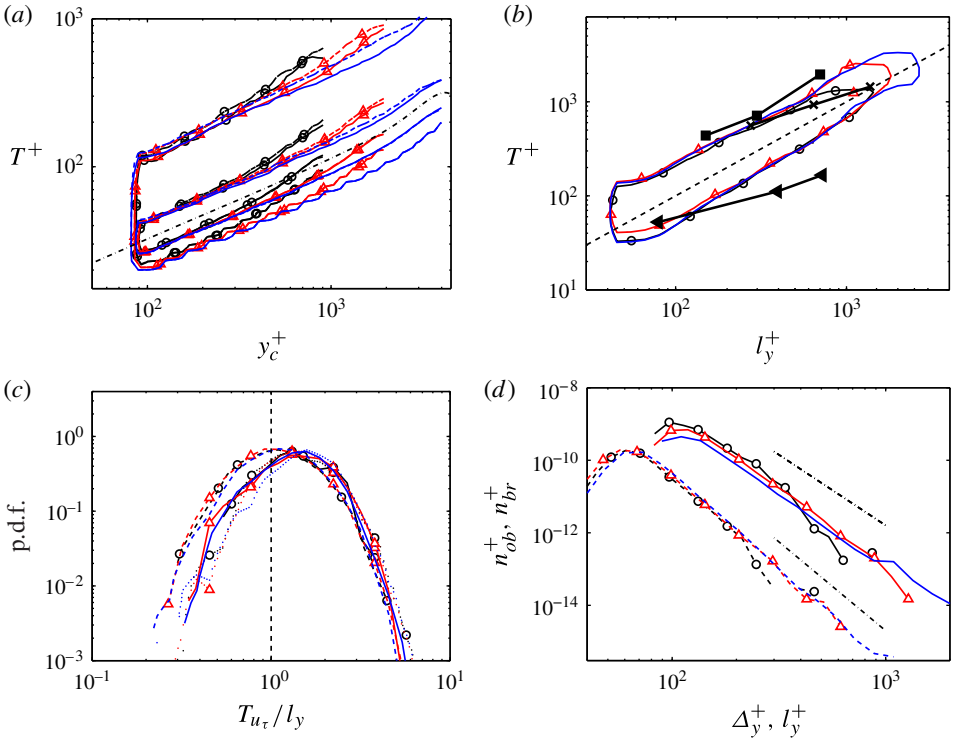

FIGURE 9. (Colour online) (*a*) Probability density functions of the lifetimes of detached Q^- primaries as a function of the height of their mean centre of gravity, y_c. Each vertical section is a p.d.f., and contours are 50 and 98 % of the maximum at each height. ——, Ejections; - - - -, sweeps; – – – – –, $T = 5t_\eta(y_c)$. (*b*) Probability density functions of the lifetimes of tall attached Q^- primaries, as a function of the mean branch height, l_y. Each vertical section is a p.d.f., and contours are 50 % of the maximum at each height. The dashed straight line is $T^+ = l_y^+$. ◀, lifetimes defined by the decay of the frequency–wavenumber spectrum of v, as computed by del Álamo *et al.* (2006) for $Re_\tau = 550$–2000; (×, ■), bursting time scale in a minimal box for the range $y/h = 0.1$–0.3, at $Re_\tau = 1880$. ■, from the temporal spectrum of the energy-production balance (Flores & Jimenez 2010); ×, from the temporal autocorrelation of v^2 (Jiménez 2013*b*). (*c*) Probability density functions of the lifetimes of tall attached primaries, normalized with the local eddy turnover. ——, Ejections; - - - -, sweeps; · · · · · · , clusters. The vertical dashed line is $Tu_\tau/l_y = 1$. (*d*) Number density per unit height, wall area and total time, of objects belonging to tall attached Q^- branches as a function of Δ_y (solid), and of the branches themselves, as a function of their height l_y (dashed). The chain-dotted lines are $n_{ob} \propto \Delta_y^{-3.7}$ and $n_{br} \propto l_y^{-4.7}$. Symbols as in table 1.

in space, but also in time. Estimates for the lifetime of the structures have been reported before, and some of them are included in figure 9(*b*), for comparison. All of them refer to the temporal evolution of some flow quantity as a function of the wall distance, not to individual structures, and we have used the correspondence $y = l_y/2$. The two lines representing temporal correlations in minimal channels agree relatively well with the present estimates, which is to be expected since they were both computed from box-averaged data, which should represent the characteristics of the largest structure present in those small boxes. The best agreement is with

the line marked with crosses (Jiménez 2013*b*), which represents the width of the temporal autocorrelation function of the box-averaged v^2, and should thus be closest to the lifetime of individual sweeps or ejections. All of the points in the line fall within the levels selected for the p.d.f.s but with a lower slope. Since only three points are available for the line, it is difficult to quantified the importance of such difference. The solid squares were obtained from the temporal spectrum of the integrated instantaneous energy balance, and are slightly longer than the present results ($3l_y/u_\tau$ versus l_y/u_τ), presumably reflecting the difference between the life of a given structure and the average period between the generation of consecutive ones (Flores & Jimenez 2010). On the other hand, the times represented by solid triangles are shorter than the present estimates. They were obtained by del Álamo *et al.* (2006) from the decorrelation time of the frequency–wavenumber spectrum of v (Wills 1964), and thus include contributions from small scales that are bound to decay faster than the larger attached structures. It was already noted by Flores & Jimenez (2010), in discussing the same data, that the definition of lifetime depends on the particular quantity being analysed and should only be taken as indicative. The present lifetimes are shorter than the periods reported by Elsinga & Marusic (2010) for the averaged orbits in the plane of Q–R invariants. These differences are not so important if we take into account that the periods of the orbits and the lifetimes presented here are computed using very different methods. In any case, the results are comparable if our structures are not expected to live for a full revolution of the orbit but just a fraction of it.

Other estimates are harder to compare. The increase of the lifetimes with the distance from the wall was noted qualitatively by LeHew *et al.* (2013), who tracked swirling structures with dimensions comparable with individual vortices in wall-parallel sections of a relatively low-Reynolds-number boundary layer ($Re_\tau = 410$). Their lifetime distributions are dominated by very short values that the authors attribute to structures moving out of the observation plane. If they are disregarded, their distributions have longer exponential tails whose decay rate imply average lifetimes that increase from $T^+ = 11$ at $y^+ = 33$ to $T^+ = 16$ at $y^+ = 200$. Even though those distributions include lifetimes up to 10 times longer than their means, these values are quite shorter than ours, especially above the buffer layer. Our distributions are also far from exponential, and the conclusion by LeHew *et al.* (2013) that the lifetimes of the detached eddies are longer than those of the attached ones contradicts the present ones. However, it should be stressed that LeHew *et al.* (2013) could only distinguish attached from detached structures indirectly.

Note that, since the local mean shear in the logarithmic layer is $S(y) \approx u_\tau/\kappa y$, where κ is the von Kármán constant, the linear growth of the lifetime with the height of the structures can be interpreted as $ST \approx 5$, which is consistent with our interpretation in figure 8 that tall branches are controlled by their interaction with the local shear (Jiménez 2013*b*). If we take this to mean that the interaction with the wall is only indirect, it would suggest that sweeps and ejections should be essentially mirror images of one another. Figure 9(*b*) is an accumulated distribution for both types of structures, but they are separated in figure 9(*c*), which reveals that the long end of the two p.d.f.s is actually very similar, but that sweeps are somewhat more likely to have short lifetimes than the ejections do. It turns out that this difference is restricted to the neighbourhood of the buffer layer. Figure 9(*d*) shows that most attached structures live near the wall, so that most of those classified as tall ($y^+_{max} > 100$) barely exceed that height. We will see below that sweeps generally approach the wall, while ejections move away from it, so that a sweep born near the top of the

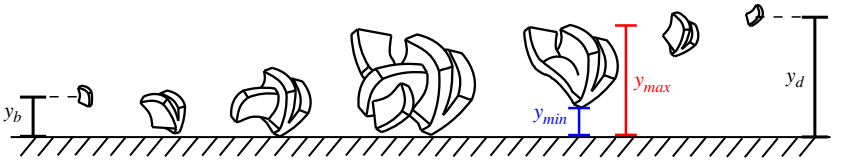

FIGURE 10. (Colour online) Sketch of the temporal evolution of a primary branch and the wall-normal position of its birth and death, respectively y_b and y_d, and the time-dependent maximum and minimum heights, y_{max} and y_{min}, of the instantaneous structure.

buffer layer tends to move near the wall and is dissipated by viscosity, while a similar ejection tends to move away from the wall and survives longer. The short-end tail of the p.d.f.s in figure 9(*c*) is due to this effect. When only taller branches are considered, the difference between sweeps and ejections decreases, and it essentially disappears for $l_y^+ > 200$. Vortex clusters behave very similarly to ejections.

In addition to the distribution of the number of structures associated with tall attached branches, figure 9(*d*) also shows the distribution of the number of branches as a function of l_y. It follows from the previous discussion that, if the number of objects decays as $n_{ob} \sim \Delta_y^{-n}$, and the lifetime of a branch is $T \sim l_y$, the number of branches should decay like $n_{br} \sim l_y^{-(n+1)}$, because each branch contributes T objects to n_{ob}. This estimate, which also assumes that the distribution of object sizes within a branch is described by the single parameter l_y, is tested in figure 9(*d*), and works well. That figure also shows that the number density of branches and objects is independent of the Reynolds number when expressed in consistent units.

As a final remark, the simulations presented here were run for at least $10h/u_\tau$, whereas the longest lifetime identified for the structures in the logarithmic layer is five times shorter, giving us some confidence on the statistical relevance of our results.

5.2. *Birth and death, and vertical evolution*

The distribution of branch births and deaths is interesting, even if only because there are at least two competing models for the genesis of tall attached structures. They differ mostly in their view of the importance of the wall. One view is that the buffer layer is the source of attached coherent motions, from where they rise into the outer region (Adrian *et al.* 2000; Christensen & Adrian 2000; Adrian 2007; Cimarelli, de Angelis & Casciola 2013). A different view, with some support from the discussion in the previous section, is that structures are controlled by the shear, and can be born at any height. In this view, the wall is mainly a source of shear, and the structures attach to it as part of the natural growth of eddies in any shear flow (Rogers & Moin 1987). Because the shear is strongest near the wall, that is also where most structures are born and are strongest, but large structures would predominantly be expected to arise farther away (del Álamo *et al.* 2006; Flores *et al.* 2007; Lozano-Durán *et al.* 2012). Figure 11(*a*,*b*) show the p.d.f.s of the height of the centres of primary Q^-s at the beginning and the end of their lives, classified as a function of the mean branch height (see the sketch in figure 10). It turns out that Q2s are born in the buffer layer, and rise, while Q4s are born away from the wall, and drop. Moreover, it appears that ejections die and sweeps are born near their mean branch height, which for attached branches is essentially $l_y \approx 2y_c$.

The evolution of the maximum and minimum structure heights during the life of a branch is given in figure 11(*c*,*d*). As we just saw, the Q2s are born attached to, or very

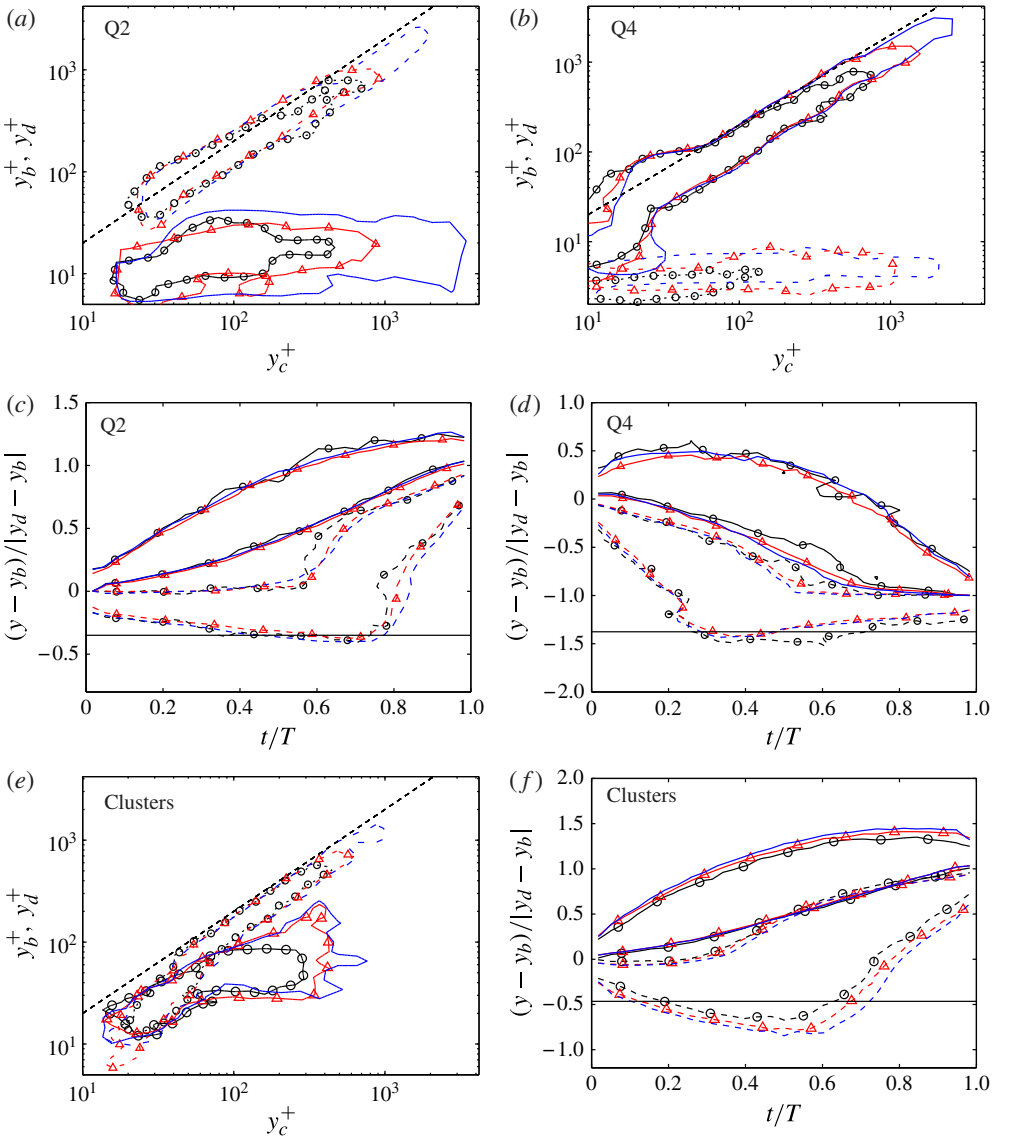

FIGURE 11. (Colour online) (*a*,*b*,*e*) Probability density functions of the wall-normal height of births, y_b (——), and deaths, y_d (- - - -), of tall attached primary branches, as a function the mean height of their centre of gravity, y_c. The dashed straight line is $y_{b,d} = 2y_c$. (*c*,*d*,*f*) Probability density functions of the minimum (- - - -) and maximum (——) heights of tall attached primary branches, as functions of the time elapsed from their birth. Time is normalized with the lifetime of each branch, T, and y_{min} and y_{max} with the heights, y_b and y_d, at its birth and death, respectively (see figure 10). The solid horizontal lines are the average position of the wall. (*a*,*c*) Ejections. (*b*,*d*) Sweeps. (*e*,*f*) Vortex clusters. In all cases, each vertical section is a p.d.f., and the contours are 0.5 of its maximum. Symbols as in table 1.

near, the wall. They remain attached for approximately $\frac{2}{3}$ of their lives, after which they detach and rise quickly. Their maximum height grows steadily during that time. The evolution of the Q4s is the opposite. Their bottom moves down relatively quickly,

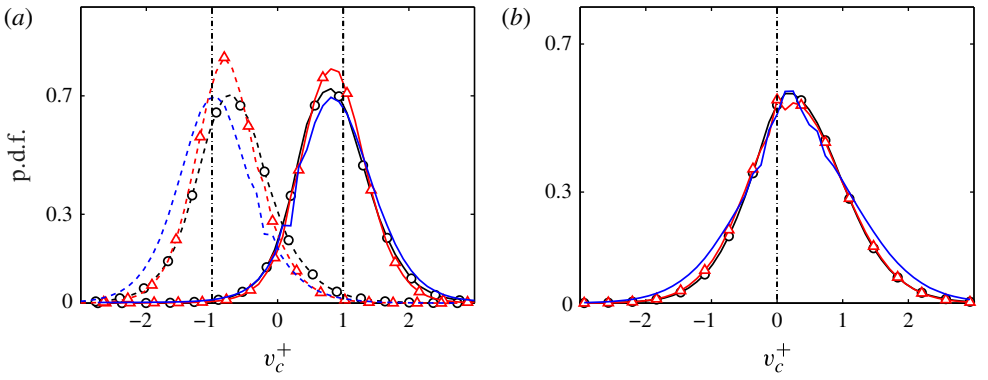

FIGURE 12. (Colour online) Probability density functions of the wall-normal velocity of the centre of gravity of the structures. The vertical lines are $\mathrm{d}y_c/\mathrm{d}t = \pm u_\tau$ in (*a*) and $\mathrm{d}y_c/\mathrm{d}t = 0$ in (*b*). (*a*) ——, Ejections; - - - -, Sweeps. (*b*) Vortex clusters. Symbols as in table 1.

attaches to the wall at roughly $\frac{1}{3}$ of the branch live and stays attached thereafter. Their top moves down steadily. The details of the distribution into attached and detached behaviour change slightly when considering very tall branches, or those closer to the buffer layer, but the overall behaviour is always just as described. Clusters behave approximately as Q2s, although, as already mentioned, their range of heights is more limited (figure 11*e*,*f*).

The wall-normal velocity of the individual eddies is shown in figure 12(*a*,*b*), defined from the vertical displacement of their centre of gravity between consecutive times separated by $\Delta t^+ \approx 30$ (to avoid spatial and temporal resolution issues) during which merging or splitting is not taking place. Consistent with the previous discussion, ejections move upwards on average, and sweeps move towards the wall, and it is interesting that both move within fairly narrow ranges of wall-normal velocities close to $\pm u_\tau$. This agrees with the results of Flores & Jimenez (2010), who noted that strong sweeps and ejections in a small channel move across the logarithmic layer with surprisingly constant velocities. Note that these velocities are also consistent with a total vertical excursion of order l_y (figure 11*a*,*b*) during a lifetime of order l_y/u_τ (figure 9*b*). Vortex clusters have both positive and negative vertical velocities. Apparently, although most clusters follow ejections as they rise, some of them also move with the sweeps as they drop. The shapes of the velocity distributions do not depend much on the attached or detached character of the structures being tracked, although the velocities decrease somewhat in the buffer layer, as expected (not shown).

It was speculated by Flores & Jimenez (2010) that bursts and ejections are parts of a single underlying structure, because they tend to burst and ebb concurrently in channels whose dimension has been adjusted to be minimal in the logarithmic layer, and also because their symmetric vertical velocities suggest a common cause. It is also known that they tend to occur in side-by-side pairs (Lozano-Durán *et al.* 2012) and that the conditional mean flow field of such pairs is a large-scale streamwise roller whose up- and down-welling edges contain the Q^-s, both in the buffer layer (Guezennec *et al.* 1989) and farther from the wall (Jiménez 2013*b*). The symmetry of the distributions in figures 9(*c*) and 12(*a*) further supports that view.

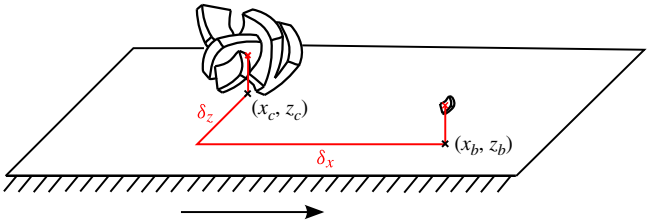

FIGURE 13. (Colour online) Sketch of the relative streamwise and spanwise distances of births with respect to existing tall attached structures. Points (x_c, z_c) and (x_b, z_b) are the wall-parallel coordinates of the centres of gravity of the existing and newborn structures, respectively.

5.3. *Relative position of branch creation*

We next consider whether the birth of new tall attached branches is influenced by pre-existent structures in their neighbourhood, such as would be the case, for example, in the vortex-packet propagation mechanism proposed by Tomkins & Adrian (2003). Note, however, that such an association would not necessarily imply causation, and could rather be due to the presence of a larger undetected common structure, as discussed above.

For that purpose, we look at the location with respect to existing structures of the birth of branches that will eventually become tall attached. At each moment, a frame of reference is defined at the centre of gravity of existing tall attached structures, and the relative positions of births taking place at that moment are computed. Figure 13 sketches the procedure. The relative distances are defined as

$$\delta_x = \frac{x_b - x_c}{\sqrt{\Delta_x^2 + \Delta_z^2}}, \tag{5.1}$$

$$\delta_z = \frac{z_b - z_c}{\sqrt{\Delta_x^2 + \Delta_z^2}}, \tag{5.2}$$

where x_c and z_c are the coordinates of the centre of the existing structure, and x_b and z_b the position of the newborn one. The distances are normalized with the length of the x–z diagonal of the circumscribed box of the existing structure, and only births between the wall and the maximum height of the existing structure are considered.

The resulting p.d.f.s are shown in figure 14(*a–d*). In all cases, the central part of the p.d.f.s has a low probability of finding births, because that region is already occupied by the existing structure. Figure 14(*a*,*b*) show that existing ejections trigger new ejections ahead of themselves, while existing sweeps trigger new sweeps predominantly behind. The p.d.f.s of the relative wall-normal position of births (not shown) reveal that the new ejections tend to appear in the buffer layer (consistently with figure 11(*a*)) whereas sweeps are born roughly at the same height as the centre of gravity of the already existing ones. Figure 14(*c*) displays the birth of sweeps with respect to existing ejections, and a symmetric figure can be drawn for ejections with respect to sweeps. It shows that Qs of different quadrants are not created aligned to each other, but side by side. Note that, in this case, the probability map is oriented in such a way that the closest newborn structure is always to the left ($\delta_z > 0$) of the existing one. An un-oriented p.d.f. would show new structures appearing symmetrically at both sides of the centre. Note also that, for that reason,

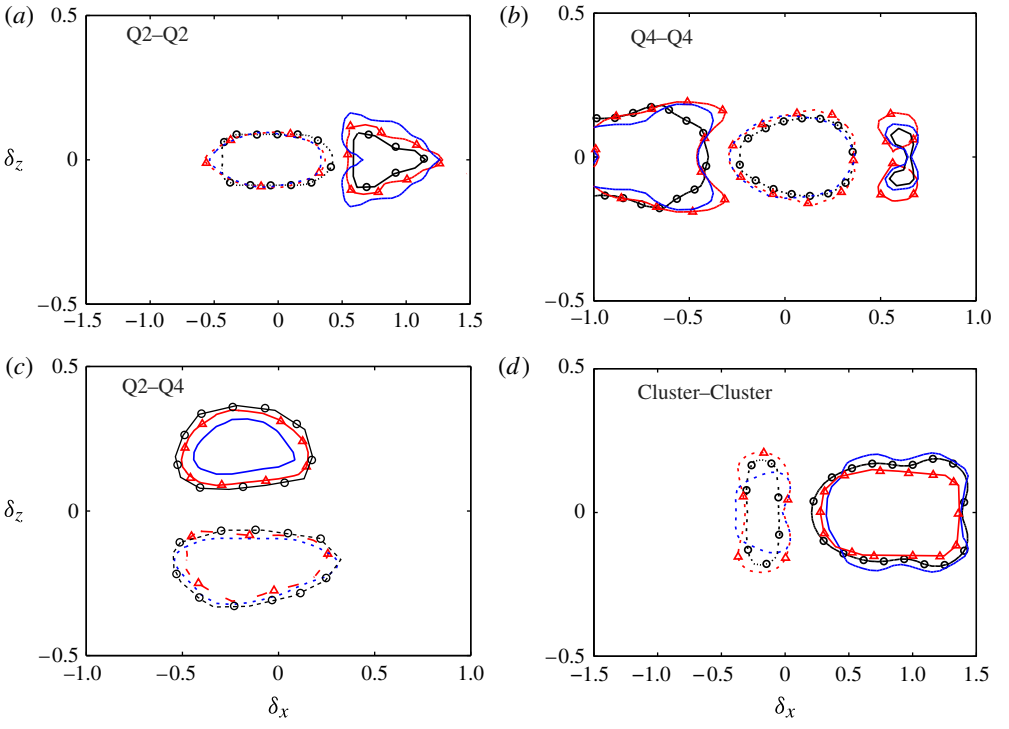

FIGURE 14. (Colour online) Joint probability density functions of the relative streamwise, δ_x, and spanwise, δ_z, distances of births with respect to existing tall attached structures whose height is $\Delta_y^+ \geqslant 200$ (see sketch in figure 13). (*a*) New ejections with respect to existing ejections. (*b*) New sweeps with respect to sweeps. (*c*) New sweeps with respect to ejections. (*d*) New vortex clusters with respect to existing clusters. Contours are 1.2 (——) and 0.8 (- - - -) the probability in the far field. Symbols as in table 1.

the minimum birth probability of this case is not at the centre of the p.d.f. but to its right ($\delta_z < 0$). Births in that location have been transferred to the peak on the left ($\delta_z > 0$). Finally, figure 14(*d*) shows that vortex clusters are born downstream of existing ones, as in the case of ejections.

The p.d.f.s in figure 14 are self-similar plots normalized with the size of the 'parent' structure, and therefore have no absolute dimensions associated with them. If we consider them as reflecting a causal relation, they show that larger structures influence regions farther from their centres than small ones do. The p.d.f.s in figure 14 are highly reminiscent of the p.d.f.s of the relative location of neighbouring structures in figure 11 of Lozano-Durán *et al.* (2012), including similar distances between the different peaks, suggesting that the geometric relations between existing structures reflect their process of formation. We have already mentioned that Q2s and Q4s are organized into streamwise trains of pairs each of which contains a Q2 and a Q4 side by side, which can be interpreted to mean that sweeps and ejections are reflections of quasi-streamwise large-scale rollers, embedded in the longer streaks of the streamwise velocity; sweeps in the high-velocity side of the streak, and ejections in the low-speed part. Figure 14(*c*) and its counterpart in Lozano-Durán *et al.* (2012) would then reflect the spanwise separation between the high- and low-velocity component of the streaks. The streamwise separation in figure 14(*a*,*b*) would correspond to the

streamwise wavelength of the inhomogeneity of the streak, which is known to take predominantly the form of meandering, both near the wall (Jiménez *et al.* 2004) and in the logarithmic layer (Hutchins & Marusic 2007).

However, the front-to-back asymmetry in figure 14(*a*,*d*) provides additional information beyond that contained in the relative position of the instantaneous structures. It shows that trains of ejections and clusters grow streamwise by extending downstream, but that sweeps grow towards their backs. This difference is difficult to interpret, since it was shown by Lozano-Durán *et al.* (2012) that there are very few unpaired Q^-s in the channel, and the Q4s triggered behind the pre-existing Q4 in figure 14(*b*) would eventually require the formation of new Q2s, and vice versa. It is not clear from figure 14(*a*) where those Q2s are coming from. Some possibilities suggest themselves, although they are unfortunately difficult to test statistically. The simplest one is probably that the pairs are completed by untriggered structures. The probability contours in figure 14 are only 20 % higher or lower than the uniform background probability of finding a newborn structure anywhere, but it is difficult to see why only one component of the organized pairs in figure 14(*c*), or in Lozano-Durán *et al.* (2012), should be created randomly. A more likely possibility is that the missing trailing Q2s are created too far from the origin to show in figure 14(*a*). A plausible variant of that scenario starts by assuming that the triggering Q2s and Q4s are always in the form of pairs. They would also trigger new pairs, but only (or predominantly) with the opposite orientation to that of the existing one. A triggering Q2 from 14(*a*) with a Q4 to its right would create ahead of itself a new Q2 with a Q4 to its left, which would be too far from the existing Q4 to appear in the conditional probability distribution in 14(*b*). A similar scenario would account for the formation of a companion Q2 for the new Q4 in figure 14(*b*). Thus, a clockwise quasi-streamwise roller, with the sweep to the right of the ejection (see figure 9 in Jiménez 2013*b*) would only trigger anticlockwise rollers ahead or behind itself. This process would not be too different from the self-propagation of hairpin packets in Tomkins & Adrian (2003), although it should be made clear that the objects being discussed here live predominantly in the logarithmic layer, and that none of the evidence in this paper, or in the companion one by Lozano-Durán *et al.* (2012), suggests the presence of hairpins in that region. Note that the generation of rollers of alternating sign along a streak leads naturally to the observed streak meandering. It also agrees with the staggered-vortex models proposed by Schoppa & Hussain (2002) for the buffer layer, and with the majority of the equilibrium and periodic exact solutions more recently found in wall-bounded flows, and reviewed, for example, by Kawahara *et al.* (2012).

5.4. *Advection velocities*

How structures deform during their evolution, and presumably what determines their lifetime, is in part controlled by the vertical gradient of their advection velocity. It is well-known that most flow variables advect roughly with the local mean streamwise velocity (Kim & Hussain 1993; Krogstad *et al.* 1998), and are thus deformed by the mean shear.

In this paper, the advection velocity of the wall-parallel sections of the structures is measured in two independent ways. In the first, the set of points within the section of the structure is correlated between consecutive times separated by $\Delta t^+ \approx 10$ (to avoid grid resolution issues), and the velocity is estimated from the shift away from the origin of the maximum correlation peak (Kuglin & Hines 1975; Sutton *et al.*

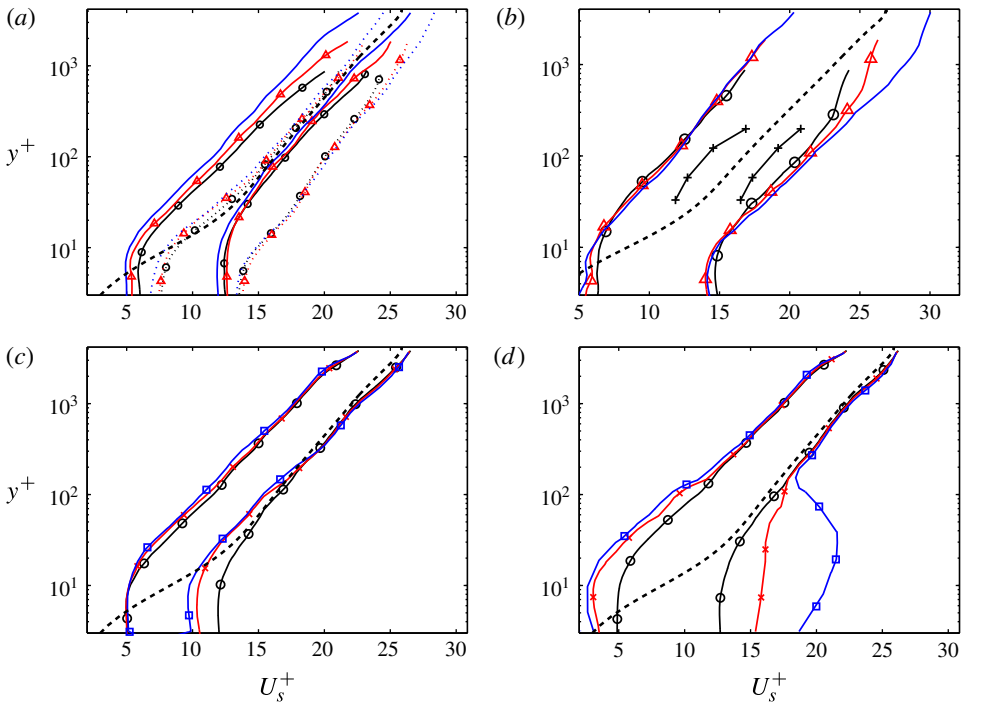

FIGURE 15. (Colour online) Probability density functions of the streamwise advection velocities of wall-parallel sections of the individual structures, as functions of their wall-normal distances. (*a*) Phase velocity. ——, Q2s; - - - -, Q4s. (*b*) Phase velocity. Vortex clusters. Symbols as in table 1. +, advection velocity of the swirling coherent structures adapted from figure 10(*b*) of LeHew *et al.* (2013). (*c*) Phase velocity. Q2s in M4200. ○, all structures; ×, $\Delta_y^+ > 400$; □, $\Delta_y^+ > 1000$. (*d*) As in (*c*), but group velocity. In all panels, each horizontal section is a p.d.f., and contours are 40 % of its maximum. The thicker dashed line is the mean streamwise velocity profile for case M4200.

1983). This is the method typically used in PIV (Willert & Gharib 1991). The second method tracks the centre of gravity of the circumscribing rectangle to the section of the structure. Both velocities need not coincide if, for example, the structure moves by accreting new elements from the front and shedding them from behind. The difference is akin to the distinction of phase and group velocity in wavepackets, with the correlation method representing the phase velocity. Non-dispersive structures in which the phase and group velocities coincide can be considered as 'coherent' objects advected by the flow, while dispersive ones are probably better understood as being 'footprints' continuously destroyed and reformed by some global influence, such as pressure.

The results are shown in figure 15(*a*,*b*), which displays phase velocities from snapshots not involved in mergers or splits. All structures move approximately with the mean profile above the buffer layer. Ejections move slightly more slowly, roughly by $-1.5u_\tau$, while sweeps move faster by roughly the same amount. This agrees with previous results (Guezennec *et al.* 1989; Krogstad *et al.* 1998), and with the idea that ejections live in low-velocity streaks, and sweeps in high-velocity streaks. Vortex clusters can be either faster or slower than $U(y)$, although the latter is slightly more probable, presumably reflecting their preferential association with ejections. This was

also seen in their vertical velocities in figure 12(*b*). Their mean advection velocity is $U(y) - 0.8u_\tau$. Close to the wall, all structures advect roughly at $10u_\tau$, in agreement with Kim & Hussain (1993) and Krogstad *et al.* (1998). Figure 15(*b*) also includes the p.d.f.s of the advection velocities reported by LeHew *et al.* (2013) which shows shorter tails although reasonable considering the differences between both methods. Elsinga *et al.* (2012) observed a mean advection velocity of $0.78U_e$ at $y = 0.2h$, with U_e the free-stream velocity of the boundary layer, which also agrees with the value of $0.776U_c$ obtained for vortex clusters at $y = 0.2h$ in the present study, being U_c the mean channel velocity at the centreline.

On the other hand, these results are not entirely consistent with those of del Álamo & Jiménez (2009), who showed that large structures with wavelengths $\lambda_x \gtrsim 2h$ advect at all heights with the bulk velocity of the mean profile, including near the wall, where that velocity is very different from the local one. Their method computes a phase velocity, and this dependence on the wavelength suggests that, at least for large attached structures near the wall, turbulence should be dispersive. The same conclusion could be drawn from the attached-eddy model of Townsend (1961), who proposed that large structures near the wall are passive ('inactive'), controlled by active cores farther away from the wall. Bradshaw (1967) later showed that the interaction between the outer active part and the inactive inner one was most likely due to the pressure induced by the active cores. This was even more vividly shown by Tuerke & Jiménez (2013) by means of a numerical experiment in which the y-distribution of the total tangential stress in a channel was modified by a distribution of volume forces. They expressed the average stress at a given distance from the wall as a y-dependent friction velocity, $u_\tau(y)$, and showed that, while the intensity of the velocity fluctuation spectrum $k_x E_{uu}(\lambda_x, y)$, where $k_x = 2\pi/\lambda_x$, scale with $u_\tau^2(y)$ for relatively short wavelengths, $\lambda_x \approx y$, the longer wavelengths scale everywhere much better with u_τ^2 at the height of the active cores, $y = \lambda_x/10$. The suggestion in all of these cases is that, while the smaller scales contained within the attached root of a large structure may move approximately with the local mean velocity, the structure itself should advect with a velocity closer to that of the active core near its centre of gravity. For a graphic representation of this process, see the different behaviours of the root and body of the structure in figure 5(*c*). Note that this observation reinforces and refines the evidence for the modulation of the inner layer by the outer one documented by Mathis, Hutchins & Marusic (2009).

This is confirmed in figure 15(*c*,*d*), which show the advection velocity separately for structures of three different size ranges. Figure 15(*c*), shows the phase velocity as a function of y. All of the size ranges agree, showing that the motion of the small scales traced by the correlation method is indeed independent of the size of their 'host' structure. On the other hand, the group velocities in 15(*d*), computed by tracking the circumscribing box, depend on the structure size. All of the structures travel with the mean velocity for $y^+ \gtrsim \Delta_y/4$, but they decouple from the mean flow below that level, and move with what can be interpreted as the advection velocity of the base of the active part of the structure. Note that, since both the shear time, $(\partial_y U)^{-1} \sim \kappa y/u_\tau$, and the local eddy-turnover time, y/u_τ, decrease as we approach the wall, such a decoupling between the top and bottom parts of the attached structures, with very different local time scales, should probably have been expected.

The conclusion that only the upper part of the tall attached structures can be considered as coherent is interesting, because the lifetime of a structure is most probably limited by its deformation by the shear. Whenever a structure is sheared by much more than its length, it should disappear as a coherent object. The difference

between the phase velocities at the top and bottom of an attached structure is approximately $\Delta U \approx u_\tau \kappa^{-1} \log \Delta_y^+$, which would shear it by an amount roughly equal to its length in a time of the order of $\Delta_x/\Delta U \sim \Delta_x/(u_\tau \log \Delta_y^+)$. This estimate differs from the data in § 5.1 by the non-trivial logarithmic denominator. On the other hand, if the only deformation that counts is that between $y = \Delta_y$ and $y = \Delta_y/4$, or some other constant factor, the shear time would be proportional to $(\Delta_x/u_\tau) \log 4$, which agrees better with the observations.

6. Secondary branches and graphs

6.1. *Graphs*

The discussion in the previous sections deals mostly with primary branches. Here we describe the behaviour of the secondary branches that interact with them. The underlying goal is to describe, if possible, the inertial cascade as a spatially localized process in which individual eddies merge and split, as implied in the original descriptions by Richardson (1920) and Obukhov (1941), rather than simply as the conceptual scale-by-scale model introduced by Kolmogorov (1941). Our tool will be the identification of such interactions within the organization of the structures into branches and graphs.

As discussed in § 4, graphs are collections of branches that interact with each other at some point in their life. It is difficult to define unique descriptors for the geometry of the graphs, which can be quite complex objects (see figure 5*a*,*b*), but they can be classified in the same way as branches. For example, a graph is tall attached if that is the case for at least one of the structures in one of its branches. For the same reasons as in the case of structures and branches, graphs can be given a unique type. For example, a Q2 graph is exclusively formed by Q2 structures, and there are no mixed graphs.

Figure 16 shows the normalized histogram of the number of branches per graph, and gives an idea of their complexity. The mode of the histogram is located at one branch per graph, but these cases correspond to simple small structures that evolve without splitting or merging. On the other hand, the tails of the histograms include large graphs with thousands of branches which represent groups of eddies (either Qs or clusters) that merge and split often, as in the example in figure 5(*a*).

Graphs are mostly made of primary, incoming and outgoing branches, with very few connectors (see the classification in figure 6 and the discussion in § 3). When incoming and outgoing branches are considered, the results obtained in previous sections are little affected for detached and buffer-layer branches, but those for tall attached ones change. Roughly 60–70 % of the tall attached branches are secondary (either incoming or outgoing). Their evolutions are truncated versions of the tall attached primaries, with lifetimes biased towards shorter values and of the order of $l_y/(2u_\tau)$, which is half of that obtained for primaries. Their minimum and maximum wall distances (not shown) behave like those presented for primary branches in figure 11(*c*,*d*,*f*) but only until they interact (merge or split) with a primary. Hence, the equivalent plots for incoming branches are similar to the first half of figure 11(*c*,*d*,*f*) from $t/T = 0$ (when they are born) to $t/T \approx 0.5$ (when they merge with a primary), whereas the plots for outgoing branches resemble the second half, from $t/T \approx 0.5$ (when they split from a primary) to $t/T = 1$ (when they die).

6.2. *Cascades*

Figure 17 contains sketches of the two basic interactions among branches, and defines the notation for this section. Each elementary interaction involves three objects. Two

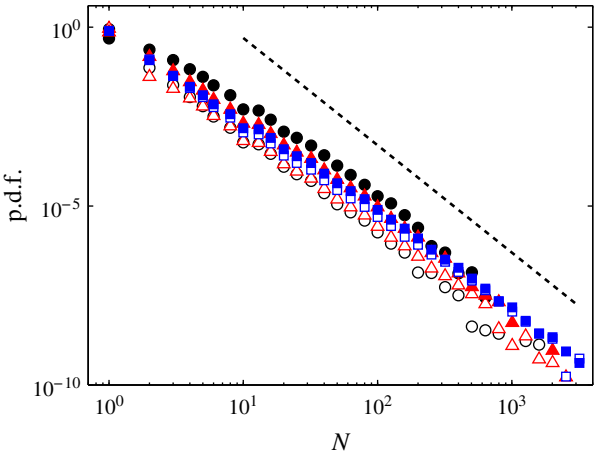

FIGURE 16. (Colour online) Probability density functions of the number of branches per graph. Open symbols for Q$^-$s and closed ones for vortex clusters. Symbols as in table 1 with squares for case M4200. The dashed line is proportional to N^{-3}.

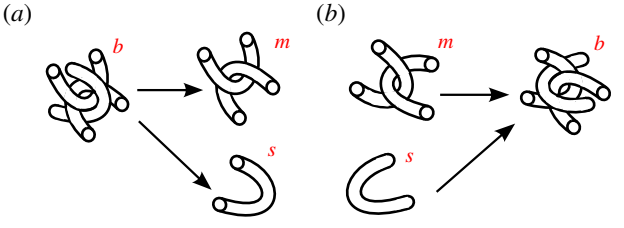

FIGURE 17. (Colour online) Sketch of the process of: (*a*) split or direct cascade and (*b*) merge or inverse cascade. The structures labelled as *b* (big) and *m* (medium) belong to the same branch, and that denoted by *s* (small) is the fragment that has split or merged.

of them, *b* for big and *m* for medium, are part of the main branch involved in the interaction, while the third (*s* for small) is the fragment being lost or gained. Thus, in the split in figure 17(*a*), a structure of characteristic size Δ_b breaks into a fragment of size Δ_m, which continues the branch, and loses a fragment of size Δ_s. We will call this interaction a direct cascade event. Similarly, in the inverse cascade event in figure 17(*b*), two structures of sizes Δ_m and Δ_s merge into a single one of size Δ_b. In both cases, the notation is $(b) \rightleftharpoons (s) + (m)$. Usually, but not always, $\Delta_b > \Delta_m > \Delta_s$. Note that the sketches in figure 17 depict the merger or split of a single structure at a given moment, but that it is fairly common to find several mergers or splits, or a mixture of them, coinciding in a single event.

For the purpose of characterizing interactions, we use as eddy size the length, Δ, of the three-dimensional diagonal of its circumscribing box, which is, on average, 1.3 times larger than the streamwise length. This choice was preferred instead of other lengths based on the volume of the structures due to their complicated shapes (see, for example, figure 2). For that reason, the split of a structure in two fragments with similar characteristic lengths as defined above do not necessarily imply similar volumes. The length Δ can be generalized to branches by averaging over the branch

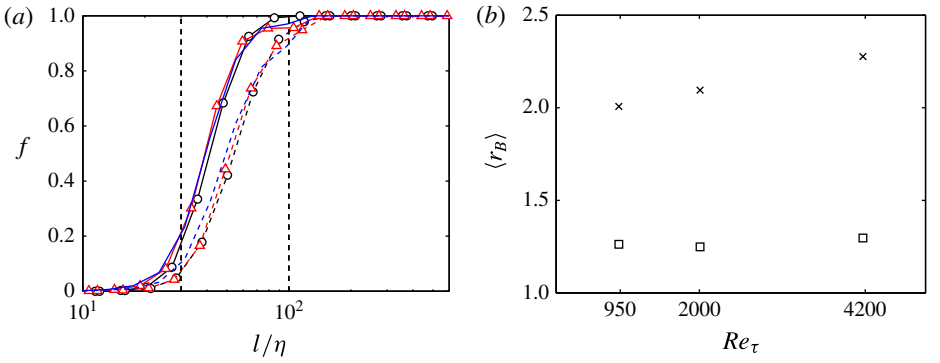

FIGURE 18. (Colour online) (*a*) Fraction, f, of the number of primary clusters branches that split (——) or merge (- - - -) at least once in their lives, as a function of the mean diagonal length of the branch, l. The buffer layer branches are excluded. The vertical dashed lines are $l = 30\eta$ and $l = 100\eta$. Symbols as in table 1. (*b*) Ratio between the volume of direct and inverse cascade as a function of the Reynolds number. □, Q$^-$s; ×, vortex clusters.

life, $l = \langle \Delta \rangle_B$, as in § 4. When normalizing it with the Kolmogorov scale, we use the channel average at the height of the centre of gravity of the branch.

Also, since very few differences were found in the cascade statistics of sweeps and ejections, they are treated together for the rest of this section.

We analyse first the prevalence of interactions. Figure 18(*a*) shows the fraction of primary vortex-cluster branches that split or merge at least once in their lives, as a function of their mean diagonal length. There is a minimum size, $l \approx 30\eta$, roughly agreeing with the peak of the energy-dissipation spectrum at $\lambda_x \approx 40\eta$ (Jiménez 2012), below which branches rarely merge or split. In this range, the cascade is presumably inhibited by viscosity, and graphs contain a single branch that evolves without splitting or merging. On the other hand, almost all of the branches larger than $l \approx 100\eta$, most of which are tall attached, merge or split at least once. In the transition between these two limits, the direct cascade predominates, and some branches split but never merge. Similar results are obtained for Q$^-$s (not shown), although with less-pronounced differences between the direct and the inverse cascades. The buffer layer branches are excluded from the figure 18(*a*). They cascade very little and, when they are included in the figure, the cascading fractions increase more slowly and the curves move to the right, reaching unity at $l \approx 180\eta$.

Next, we characterize the part of the growth and decay of the structures that is due to mergers and splits, which can be interpreted as a measure of the contribution of the inverse and direct cascades to the eddy evolution. To do that, we compare the total volume gained or lost by primary branches in their cascade interactions with the average volume of the branch, V_b. For example, the total lost volume (direct cascade), $\sum_B V_{sd}$, is defined as the sum of the volumes of all of the fragments lost during the life of the branch, with a similar definition for the volume gained, $\sum_B V_{si}$. Excluding the buffer layer branches, Q primaries with $l > 100\eta$ have on average $\sum_B V_{sd}/V_b \approx 0.72$ and $\sum_B V_{si}/V_b \approx 0.50$ for case M4200. For vortex clusters, the ratios are on average 1.41 and 0.73. In both cases mergers and splits are substantial contributors to the eddy growth and decay.

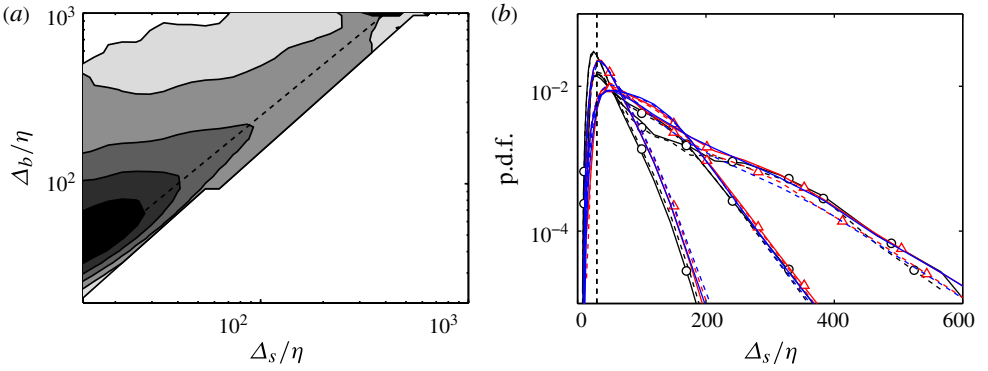

FIGURE 19. (Colour online) (*a*) Volume ratio between the direct and inverse cascades, as a function of the sizes of the smallest and largest fragments in a given interaction. Vortex clusters in M4200. The dashed line is $\Delta_s = 0.4\Delta_b$. Contours are, from dark to light, 3.5, 3, 2.5, 2 and 1.2. (*b*) Probability density functions of the sizes of the fragments merged (- - - -) or split (——), Δ_s, for different lengths of the larger eddy involved, $\Delta_b/\eta =$ 0–200, 200–500, 500–2000. Data for vortex clusters. The vertical dashed line is $\Delta_s = 30\eta$. Symbols as in table 1.

The ratio

$$r_B = \frac{\sum_B V_{sd}}{\sum_B V_{si}}, \tag{6.1}$$

gives an idea of which of the two cascades dominates in a given branch. Its average, $\langle r_B \rangle$, is plotted in figure 18(*b*) for different Reynolds numbers and branch types. The direct cascade always dominates, especially for vortex clusters, and its dominance increases slightly with the Reynolds number. However, the imbalance is not huge, approximately 1.3 for Q$^-$s and 2.2 for vortex clusters, implying that the inverse cascade is not negligible, in accordance with the backscatter observations of Piomelli *et al.* (1991) and others.

To understand better how this imbalance is distributed as a function of scale, we decompose the ratio r_B in terms of the size of the fragments involved, r. Figure 19(*a*) shows the ratio $r(\Delta_s,\ \Delta_b)$, defined as in (6.1) but restricting the sums and the subsequent averaging to interactions involving a smallest and largest eddy of those sizes. The figure refers to vortex clusters in case M4200, but qualitatively similar ones are obtained for Q$^-$s and for vortex clusters at different Reynolds numbers.

The direct cascade always prevails, but the imbalance is strongest along a ridge $\Delta_s \approx 0.4\Delta_b$, which corresponds to eddies splitting roughly in halves, or merging with others of similar size. It is also strongest for small structures below $\Delta_b \approx 60\eta$, which tend to split in fragments of $\Delta_s \approx 20\eta$ much more frequently than they merge. This ridge can be interpreted as the preferred locus of a predominantly direct cascade, but note again that the imbalance for inertial structures is at most a factor of two, and that the cascade only really becomes unidirectional when one of the fragments is small enough to be dissipated by viscosity.

Figure 19(*b*) studies in more detail the merging or splitting process by presenting the p.d.f.s of the size of the smallest structure involved in an interaction for different

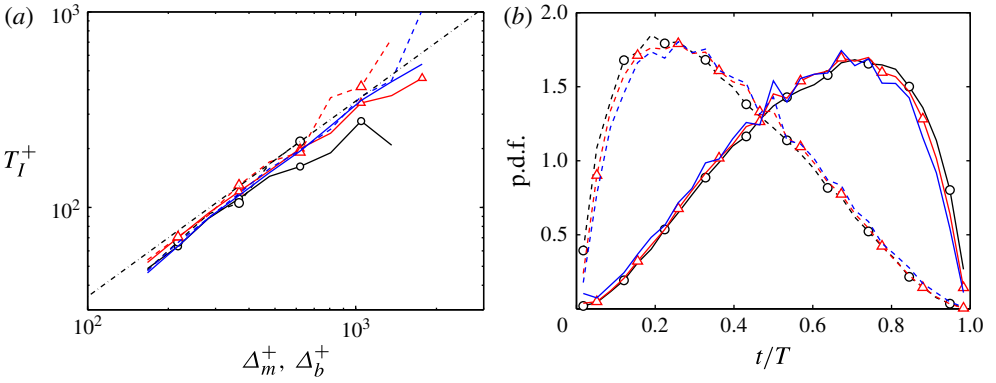

FIGURE 20. (Colour online) (*a*) Average time, T_I, for a Q$^-$ to merge with, or split into, two fragments of similar size ($|\Delta_m - \Delta_s|/\Delta_m < 0.1$), plotted against Δ_m for mergers and Δ_b for splits. ——, splitting; - - - -, merging. The dashed-dotted line is $T_I^+ = 0.35\Delta_{m,b}^+$. Data for primary branches. (*b*) Probability density functions of the time at which mergers and splits take place, normalized with the branch lifetime. ——, splits, - - - -, mergers. Primary tall attached Q$^-$s. Symbols as in table 1.

ranges of the size of largest one. Most of the fragments are of the order of $\Delta_s \approx 30\eta$, corresponding to viscous fragments torn from larger eddies or merging into them. However, the tails of the p.d.f.s get longer as the largest structure gets bigger, representing inertial interactions between eddies of comparable sizes. Further analysis of the data (not shown) confirms this trend, and reveals that the size of the largest fragment likely to merge into, or split from, an eddy of size Δ_b is some fixed fraction of Δ_b. Note that the p.d.f.s in figure 19(*b*) are almost identical for mergers and splits, and that the previous discussion applies equally well for the direct as for the inverse cascade.

The temporal behaviour of the two cascades is studied in figure 20. Figure 20(*a*) shows the average time, T_I, elapsed before a Q$^-$ of size Δ_b splits into two similar fragments, or a Q$^-$ of size Δ_m merges with another one of similar size (in both cases defined as $|\Delta_m - \Delta_s| < 0.1\Delta_m$). This time may be interpreted as characterizing the inertial cascade and it is defined as the time elapsed between the birth of a primary and its first roughly symmetrical split or merger at sizes Δ_b or Δ_m, respectively. In the case of several such events in a single branch, we consider T_I as the time between two consecutive inertial interactions, with the sizes Δ_b and Δ_m belonging to the last one. The results show that $T_I^+ \approx 0.35\Delta_{m,b}^+$ for both merging and splitting, and a further analysis reveals that primaries with $l > 100\eta$ undergo two or three inertial events in its life, counting mergers and splits. In general, if we count any interaction regardless of its size, the average number of splits (or mergers) in a branch is $n \approx 10^{-4}(l/\eta)^2$ for primaries with $l > 100\eta$ and excluding the buffer layer branches.

Figure 20(*b*) shows that mergers and splits are asymmetrically distributed during the life of the branch. While splits happen at the end of the life, and contribute to tear the structure apart, mergers take place at the beginning and enhance the early stages of the growth of the eddy. While the figure is drawn for Q$^-$s, similar results are obtained for vortex clusters.

Finally, the spatial organization of mergers and splits is studied in figure 22 by looking at the relative position of the centre of gravity of the smallest fragment with respect to the intermediate one (see the sketch in figure 21). Figure 22(*a*,*b*)

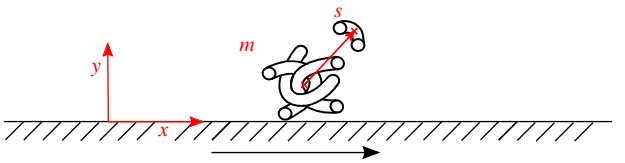

FIGURE 21. (Colour online) Sketch of the relative position of the centre of gravity of fragments merged or split (structure s) with respect to the centre of gravity of the medium eddy (structure m).

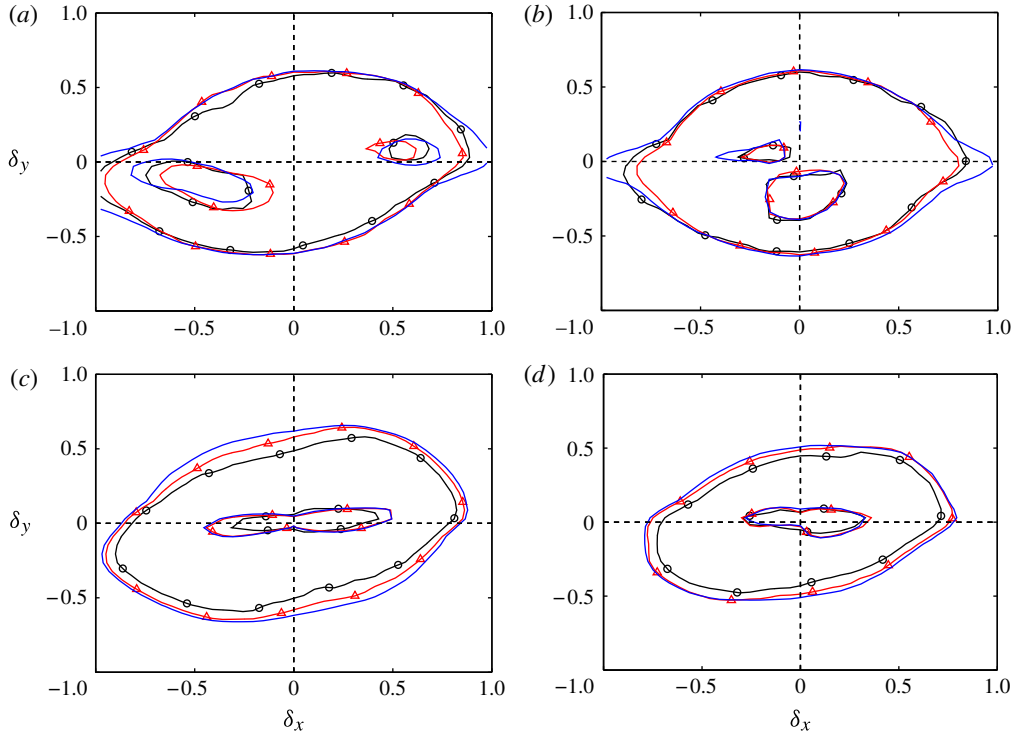

FIGURE 22. (Colour online) Joint probability density functions of the relative wall-normal and streamwise distances of the centres of mergers and splits (structures s) with respect to the centre of the medium eddy (structure m) normalized with the characteristic size of the latter, l_m. See the sketch in figure 21. Contours are 20 and 90 % of the data. (*a*) Splits for Q$^-$s. (*b*) Mergers for Q$^-$s. (*c*) Splits for vortex clusters. (*d*) Mergers for vortex clusters. Symbols as in table 1.

show results for Q$^-$s. Most of the mergers and splits take place in the streamwise direction. The structures merge predominantly with fragments below and ahead of them, presumably because taller and faster structures overtake smaller ones. The splits occur mostly in the tail of the structure or in its upper-front head. Since we saw in § 5.4 that tall attached Q$^-$s are tilted forward by the shear, this distribution of splits seem to reflect the occasional tearing of their heads and tails during that process. The results for vortex clusters are not as interesting (figure 22*c*,*d*). Most of their interactions take place near the core of the original structure. The reason is probably

that vortex clusters are much 'emptier' than Q^-s (see figure 2, and Lozano-Durán *et al.* 2012), and there is enough space within them for mergers and splits to happen internally.

With respect to the nature of the participants in an interaction, tall attached structures split 68 % of the time into another tall attached structure and either a detached or a short attached one. In 25 % of the interactions, neither of the resultant structures is tall attached, while only in 7 % of the cases both of them are. Similar results are obtained for mergers and vortex clusters at different Reynolds numbers in this respect.

Taking the evidence in this section at face value, it is difficult not to think of the classical interpretation of the cascade by Leith (1967) or Orszag (1970), according to which the inertial energy transfer is an entropy-driven random process in phase space, in which energy tends to equipartition while drifting either up or down in scale (see the discussion in Lesieur 1991, pp. 295–305). It is only when viscosity breaks the energy conservation at the smallest scales that the energy is unidirectionally drained into heat. However, there are two important caveats.

The first was already mentioned in the introduction. It should be clearly understood that most of the results in this section refer to the large scales in which energy is being fed into any possible inertial cascade. This should be clear from their association with the tangential Reynolds stress, and from the observation in figure 8 that the attached structures are larger that the Corrsin scale, and therefore directly coupled with the mean shear. As such, although the cascade process described in this section is probably a good description of how the momentum transfer changes scale across the logarithmic layer, it may not be representative of the behaviour of the, presumably universal, Kolmogorov (1941) inertial energy cascade.

In the second place, the description of a structure gaining fragments from its front (or back) while shedding them from the other end, could be interpreted as the definition of a dispersive wavepacket, and it was shown in § 5.4 that the bottom part of the attached structures is dispersive. To test whether this could be a simpler interpretation of the 'reversible' cascade described here, the objects from case M2000 were recomputed and tracked again after discarding all the planes for which $y^+ < 100$. It follows from figure 15(*d*) that structures above that level are mostly non-dispersive. The results in this section were then recalculated. The new structures were indeed different from those including the buffer layer. For example, the average structure size decreased somewhat, reflecting the loss of connectivity through the buffer layer, but no qualitative differences were found for the cascade statistics described here.

7. Discussion and conclusions

We have presented a novel approach to the study of the kinematics and dynamics of wall-bounded turbulent flows, and applied it to temporally and spatially well-resolved simulations of turbulent channels in the range of Reynolds numbers $Re_\tau = 930$–4200. The fields were stored often enough, and the simulated time was long enough, for several millions of structures to be individually tracked from birth to death. Two types of structures were analysed, vortex clusters (del Álamo *et al.* 2006) and the quadrant structures of the tangential Reynolds stress (Lozano-Durán *et al.* 2012). Although it was found that most structures of both types stay small and live short lives, special emphasis was put on the tall attached sweeps and ejections with longer lifetimes stretching from the wall into the logarithmic layer. In agreement with previous investigators, those structures were found to carry most of the wall-normal momentum transfer.

The tracking procedure resulted in the organization of the structures into primary branches, representing the evolution of a single structure from birth to death, and a complicated set of secondary branches that either merge into or split from them. Primary tall attached structures were shown to be geometrically self-similar, with roughly constant aspect ratios for branches taller than $l_y^+ > 100$–200, and equally self-similar lifetimes, $T^+ \approx l_y^+$. This was true for sweeps, ejections and vortex clusters, and it is striking that branches of sweeps and ejections were found to be essentially mirror images of each other. Both have essentially identical lifetimes, and their vertical advection velocities are antisymmetric: $+u_\tau$ for the ejections and $-u_\tau$ for the sweeps. Moreover, ejections are born near the wall and rise until they disappear near their maximum height, and sweeps are born away from the wall and move towards it. This, together with the observation by previous investigators that sweeps and ejections are typically found in side-by-side pairs (Lozano-Durán *et al.* 2012), strongly suggests that both structures are manifestations of a single quasi-streamwise roller lying between them, whose height does not change much during its evolution. Vortex clusters, which are typically found between sweeps and ejections, tend to follow the ejections, and are probably partial manifestations of the roller. Tall attached sweeps and ejections are found more often in the high-shear region near the wall, but they appear often enough at all heights for the largest structures to be responsible for most of the momentum transfer. Several observations were shown to imply that the largest structures at each height are large enough to be controlled by the shear, and their antisymmetry suggests that they are not necessarily created near the wall, but are rather a general consequence of the mean shear itself. On the other hand, detached structures are much smaller than the tall attached ones and have sizes and lifetimes of the order of the local Kolmogorov scales.

It was found that new structures form predominantly ahead or behind structures of the same kind, but the details of that process were found to be difficult to reconcile with the rest of the available evidence unless sweeps and ejections were again considered part of side-by-side pairs that trigger new pairs of opposite polarity. A clockwise roller would thus follow a counterclockwise one, and vice versa. Although our study deals mostly with large structures in the logarithmic and outer layers, the resulting model of alternating vortices flanking a streak agrees qualitatively with older ones of the buffer layer, and with transitional exact structures at much lower Reynolds numbers.

The streamwise advection velocity of individual structures was measured, and found to depend on the distance to the wall, implying that the structures are deformed enough by the mean shear that their lifetime is controlled by that deformation. It was moreover found that their group and phase velocities only coincide in the top part of the tall attached structures ($y > \Delta_y/4$). This is the only part of the structure that can be considered coherent. The 'root' below that height is dispersive, and is probably just the 'pressure shadow' of the upper core. New small structures in that region are either created or accreted at the front of the structure and shed from behind. This was interpreted to be the individual-structure counterpart of the classical active–inactive organization proposed by Townsend (1961). We have noted that restricting coherence to the upper part of the attached structures also makes their observed lifetimes consistent with a model in which they are created and eventually destroyed by their deformation by the mean velocity profile.

It was found that the interactions (merging and splitting) among branches constitute a substantial part of their evolution, and could not be neglected. We have analysed them as indicators of a cascade of the quantities carried by the structures involved;

in this case, the wall-normal momentum transfer by the sweeps and ejections, and the enstrophy by the vortex clusters, even if the latter quantity is not conserved as is the former. Following the geometrical model proposed by Richardson (1920) and Obukhov (1941) in which cascading structures are related locally in space, mergers were taken to indicate an inverse cascade, from smaller to larger sizes, and splits to represent a direct one, from large to small. This process that does not necessarily coincide with the energy cascade proposed by Kolmogorov (1941), which is local in scale space. The resulting picture is more complex than a simple direct cascade of large eddies into small ones. Eddies smaller than approximately 30η were found to cascade only rarely, while those larger than 100η almost always do. In those cases, the total volume gained and lost was found to be a substantial fraction of the total volume of the large structures. Most branch interactions were found to be the shedding or absorption of Kolmogorov-scale fragments by larger structures, but more balanced splits or mergers spanning a wide range of scales were also found to be important. Not surprisingly, mergers are more common during the initial growth part of the evolution of the structures, while splits predominate later in their life, but the contributions from both directions of the cascade are surprisingly balanced. Only those involving small viscous fragments can be described as essentially unidirectional (direct). A typical large attached eddy cascades into comparable fragments two or three times during its life.

The location of the mergers and splits with respect to the largest eddy involved in the interaction was also investigated. Large attached momentum structures, which can be roughly described as forward-leaning, add fragments from below, probably by overtaking them, and lose them from their upper head and their lower back, probably by shearing. Clusters, which are more disorganized, and with an emptier interior space, tend to cascade from the inside. These behaviours persist even when the buffer layer is discarded from the identification and tracking of individual structures, and they are therefore probably distinct from the dispersive eddy roots mentioned above.

The model proposed shares a few properties with the hairpin's packet paradigm (Adrian 2007) like being consistent with the logarithmic velocity profile and the self-similar nature of the structures involved. Nevertheless, the results reveal crucial differences that make the two models no longer compatible. The scenario proposed here is much more disorganized and the structures involved are complicated multiscale objects. If tall attached vortex clusters would be considered as markers for hairpin-like structures, most of them would be born close to the wall and rise. However, not all of the attached structures appear at the wall. Sweeps are created further away from the wall and only later move towards it. In addition, the symmetries found between tall attached ejections and sweeps with heights well above the buffer layer (i.e. the evolution of their maximum and minimum wall distances, their wall-normal velocities, their grouping in pairs, their lifetimes and sizes, etc.) diminish the importance of the wall as the main source of tall attached eddies. Regarding the casual relations between hairpins and ejections, tall attached vortex clusters do not grow in the wall-normal direction as much as the ejections do, suggesting than the latter could not be the consequence of fluid pumped by hairpins' packets but rather their cause. Other differences are also worth mentioning, such as that the merging of our structures takes place mostly in the streamwise direction rather than in spanwise, as conjectured for hairpins.

Acknowledgements

This work was supported in part by CICYT, under grant TRA2009-11498, and by the European Research Council, under grant ERC-2010.AdG-20100224. A. Lozano–Durán was supported by an FPI fellowship from the Spanish Ministry of Education and Science. The computations were made possible by generous grants of computer time from CeSViMa (Centro de Supercomputación y Visualización de Madrid) and BSC (Barcelona Supercomputing Centre).

Supplementary material

Supplementary material is available at http://dx.doi.org/10.1017/jfm.2014.575.

REFERENCES

ACARLAR, M. S. & SMITH, C. R. 1987*a* A study of hairpin vortices in a laminar boundary layer. Part 1. Hairpin vortices generated by a hemisphere protuberance. *J. Fluid Mech.* **175**, 1–41.

ACARLAR, M. S. & SMITH, C. R. 1987*b* A study of hairpin vortices in a laminar boundary layer. Part 2. Hairpin vortices generated by fluid injection. *J. Fluid Mech.* **175**, 43–83.

ADRIAN, R. J. 1991 Particle-imaging techniques for experimental fluid mechanics. *Annu. Rev. Fluid Mech.* **23** (1), 261–304.

ADRIAN, R. 2005 Twenty years of particle image velocimetry. *Exp. Fluids* **39** (2), 159–169.

ADRIAN, R. J. 2007 Hairpin vortex organization in wall turbulence. *Phys. Fluids* **19** (4), 041301.

ADRIAN, R. J., MEINHART, C. D. & TOMKINS, C. D. 2000 Vortex organization in the outer region of the turbulent boundary layer. *J. Fluid Mech.* **422**, 1–54.

DEL ÁLAMO, J. C. & JIMÉNEZ, J. 2009 Estimation of turbulent convection velocities and corrections to Taylor's approximation. *J. Fluid Mech.* **640**, 5–26.

DEL ÁLAMO, J. C., JIMÉNEZ, J., ZANDONADE, P. & MOSER, R. D. 2004 Scaling of the energy spectra of turbulent channels. *J. Fluid Mech.* **500**, 135–144.

DEL ÁLAMO, J. C., JIMÉNEZ, J., ZANDONADE, P. & MOSER, R. D. 2006 Self-similar vortex clusters in the turbulent logarithmic region. *J. Fluid Mech.* **561**, 329–358.

AOYAMA, T., ISHIHARA, T., KANEDA, Y., YOKOKAWA, M. & UN, A. 2005 Statistics of energy transfer in high-resolution direct numerical simulation of turbulence in a periodic box. *J. Phys. Soc. Japan* **74**, 3202–3212.

BERNARD, P. S. 2013 Vortex dynamics in transitional and turbulent boundary layers. *AIAA J.* **51** (8), 1828–1842.

BLACKWELDER, R. F. & KAPLAN, R. E. 1976 On the wall structure of the turbulent boundary layer. *J. Fluid Mech.* **76**, 89–112.

BOGARD, D. G. & TIEDERMAN, W. G. 1986 Burst detection with single-point velocity measurements. *J. Fluid Mech.* **162**, 389–413.

BRADSHAW, P. 1967 Inactive motions and pressure fluctuations in turbulent boundary layers. *J. Fluid Mech.* **30**, 241–258.

BROWN, G. L. & ROSHKO, A. 1974 On density effects and large structure in turbulent mixing layers. *J. Fluid Mech.* **64**, 775–816.

CADOT, O., DOUADY, S. & COUDER, Y. 1995 Characterization of the low-pressure filaments in a three-dimensional turbulent shear flow. *Phys. Fluids* **7** (3), 630–646.

CHONG, M. S., PERRY, A. E. & CANTWELL, B. J. 1990 A general classification of three-dimensional flow fields. *Phys. Fluids* **2** (5), 765–777.

CHRISTENSEN, K. T. & ADRIAN, R. J. 2000 Statistical evidence of hairpin vortex packets in wall turbulence. *J. Fluid Mech.* **431**, 433–443.

CIMARELLI, A., DE ANGELIS, E. & CASCIOLA, C. M. 2013 Paths of energy in turbulent channel flows. *J. Fluid Mech.* **715**, 436–451.

CORINO, E. R. & BRODKEY, R. S. 1969 A visual investigation of the wall region in turbulent flow. *J. Fluid Mech.* **37**, 1–30.

CORRSIN, S. 1958 Local isotropy in turbulent shear flow. Res. Memo 58B11. NACA.

DENNIS, D. J. C. & NICKELS, T. B. 2011*a* Experimental measurement of large-scale three-dimensional structures in a turbulent boundary layer. Part 1. Vortex packets. *J. Fluid Mech.* **673**, 180–217.

DENNIS, D. J. C. & NICKELS, T. B. 2011*b* Experimental measurement of large-scale three-dimensional structures in a turbulent boundary layer. Part 2. Long structures. *J. Fluid Mech.* **673**, 218–244.

ELSINGA, G. E. & MARUSIC, I. 2010 Evolution and lifetimes of flow topology in a turbulent boundary layer. *Phys. Fluids* **22** (1), 015102.

ELSINGA, G. E., POELMA, C., SCHRÖDER, A., GEISLER, R., SCARANO, F. & WESTERWEEL, J. 2012 Tracking of vortices in a turbulent boundary layer. *J. Fluid Mech.* **697**, 273–295.

FLORES, O. & JIMÉNEZ, J. 2010 Hierarchy of minimal flow units in the logarithmic layer. *Phys. Fluids* **22** (7), 071704.

FLORES, O., JIMÉNEZ, J. & DEL ÁLAMO, J. C. 2007 Vorticity organization in the outer layer of turbulent channels with disturbed walls. *J. Fluid Mech.* **591**, 145–154.

GUALA, M., HOMMEMA, S. E. & ADRIAN, R. J. 2006 Large-scale and very-large-scale motions in turbulent pipe flow. *J. Fluid Mech.* **554**, 521–542.

GUEZENNEC, Y. G., PIOMELLI, U. & KIM, J. 1989 On the shape and dynamics of wall structures in turbulent channel flow. *Phys. Fluids* **1** (4), 764–766.

HAIDARI, A. H. & SMITH, C. R. 1994 The generation and regeneration of single hairpin vortices. *J. Fluid Mech.* **277**, 135–162.

HEAD, M. R. & BANDYOPADHYAY, P. 1981 New aspects of turbulent boundary-layer structure. *J. Fluid Mech.* **107**, 297–338.

HOYAS, S. & JIMÉNEZ, J. 2006 Scaling of the velocity fluctuations in turbulent channels up to $Re_\tau = 2003$. *Phys. Fluids* **18** (1), 011702.

HUTCHINS, N. & MARUSIC, I. 2007 Evidence of very long meandering features in the logarithmic region of turbulent boundary layers. *J. Fluid Mech.* **579**, 1–28.

JIMÉNEZ, J. 1998 The largest scales of turbulence. In *CTR Ann. Res. Briefs*, Stanford University, pp. 137–154.

JIMÉNEZ, J. 2012 Cascades in wall-bounded turbulence. *Annu. Rev. Fluid Mech.* **44**, 27–45.

JIMÉNEZ, J. 2013*a* How linear is wall-bounded turbulence? *Phys. Fluids* **25**, 110814.

JIMÉNEZ, J. 2013*b* Near-wall turbulence. *Phys. Fluids* **25** (10), 101302.

JIMÉNEZ, J., DEL ÁLAMO, J. C. & FLORES, O. 2004 The large-scale dynamics of near-wall turbulence. *J. Fluid Mech.* **505**, 179–199.

JIMÉNEZ, J. & HOYAS, S. 2008 Turbulent fluctuations above the buffer layer of wall-bounded flows. *J. Fluid Mech.* **611**, 215–236.

JIMÉNEZ, J., KAWAHARA, G., SIMENS, M. P., NAGATA, M. & SHIBA, M. 2005 Characterization of near-wall turbulence in terms of equilibrium and 'bursting' solutions. *Phys. Fluids* **17** (1), 015105.

JIMÉNEZ, J. & MOIN, P. 1991 The minimal flow unit in near-wall turbulence. *J. Fluid Mech.* **225**, 213–240.

JIMÉNEZ, J. & PINELLI, A. 1999 The autonomous cycle of near-wall turbulence. *J. Fluid Mech.* **389**, 335–359.

JIMÉNEZ, J. & WRAY, A. A. 1998 On the characteristics of vortex filaments in isotropic turbulence. *J. Fluid Mech.* **373**, 255–285.

JIMÉNEZ, J., WRAY, A. A., SAFFMAN, P. G. & ROGALLO, R. S. 1993 The structure of intense vorticity in isotropic turbulence. *J. Fluid Mech.* **255**, 65–90.

JOHANSSON, A. V., ALFREDSSON, P. H. & KIM, J. 1991 Evolution and dynamics of shear-layer structures in near-wall turbulence. *J. Fluid Mech.* **224**, 579–599.

KAWAHARA, G., UHLMANN, M. & VAN VEEN, L. 2012 The significance of simple invariant solutions in turbulent flows. *Annu. Rev. Fluid Mech.* **44** (1), 203–225.

KIM, K. & ADRIAN, R. J. 1999 Very large-scale motion in the outer layer. *Phys. Fluids* **11** (2), 417–422.

KIM, J. & HUSSAIN, F. 1993 Propagation velocity of perturbations in turbulent channel flow. *Phys. Fluids* **5** (3), 695–706.

KIM, J., MOIN, P. & MOSER, R. D. 1987 Turbulence statistics in fully developed channel flow at low Reynolds number. *J. Fluid Mech.* **177**, 133–166.

KLINE, S. J., REYNOLDS, W. C., SCHRAUB, F. A. & RUNSTADLER, P. W. 1967 The structure of turbulent boundary layers. *J. Fluid Mech.* **30**, 741–773.

KOLMOGOROV, A. N. 1941 The local structure of turbulence in incompressible viscous fluid for very large Reynolds' numbers. *Dokl. Akad. Nauk SSSR* **30**, 301–305.

KROGSTAD, P.-A., KASPERSEN, J. H. & RIMESTAD, S. 1998 Convection velocities in a turbulent boundary layer. *Phys. Fluids* **10** (4), 949–957.

KUGLIN, C. D. & HINES, D. C. 1975 The phase correlation image alignment method. In *Proceeding of IEEE International Conference on Cybernetics and Society*, pp. 163–165.

LEHEW, J., GUALA, M. & MCKEON, B. 2013 Time-resolved measurements of coherent structures in the turbulent boundary layer. *Exp. Fluids* **54** (4), 1–16.

LEITH, C. E. 1967 Diffusion approximation to inertial energy transfer in isotropic turbulence. *Phys. Fluids* **10**, 1409–1416.

LESIEUR, M. 1991 *Turbulence in Fluids*, 2nd edn. Springer.

LOZANO-DURÁN, A., FLORES, O. & JIMÉNEZ, J. 2012 The three-dimensional structure of momentum transfer in turbulent channels. *J. Fluid Mech.* **694**, 100–130.

LOZANO-DURÁN, A. & JIMÉNEZ, J. 2010 Time-resolved evolution of the wall-bounded vorticity cascade. In *Proceedings Div. Fluid Dyn.*, p. EB-3. American Physical Society.

LOZANO-DURÁN, A. & JIMÉNEZ, J. 2011 Time-resolved evolution of the wall-bounded vorticity cascade. *J. Phys.: Conf. Ser.* **318** (6), 062016.

LOZANO-DURÁN, A. & JIMÉNEZ, J. 2014 Effect of the computational domain on direct simulations of turbulent channels up to $Re_\tau = 4200$. *Phys. Fluids* **26** (1), 011702.

LU, S. S. & WILLMARTH, W. W. 1973 Measurements of the structure of the Reynolds stress in a turbulent boundary layer. *J. Fluid Mech.* **60**, 481–511.

MARTÍN, J., OOI, A., CHONG, M. S. & SORIA, J. 1998 Dynamics of the velocity gradient tensor invariants in isotropic turbulence. *Phys. Fluids* **10** (9), 2336–2346.

MARUSIC, I. 2001 On the role of large-scale structures in wall turbulence. *Phys. Fluids* **13** (3), 735–743.

MATHIS, R., HUTCHINS, N. & MARUSIC, I. 2009 Large-scale amplitude modulation of the small-scale structures in turbulent boundary layers. *J. Fluid Mech.* **628**, 311–337.

MCKEON, B. & SREENIVASAN, K. 2007 Introduction: scaling and structure in high Reynolds number wall-bounded flows. *Phil. Trans. R. Soc.* A **365** (1852), 635–646.

MIZUNO, Y. & JIMÉNEZ, J. 2013 Wall turbulence without walls. *J. Fluid Mech.* **723**, 429–455.

MOISY, F. & JIMÉNEZ, J. 2004 Geometry and clustering of intense structures in isotropic turbulence. *J. Fluid Mech.* **513**, 111–133.

NICKELS, T. B. & MARUSIC, I. 2001 On the different contributions of coherent structures to the spectra of a turbulent round jet and a turbulent boundary layer. *J. Fluid Mech.* **448**, 367–385.

OBUKHOV, A. M. 1941 On the distribution of energy in the spectrum of turbulent flow. *Izv. Akad. Nauk USSR, Ser. Geogr. Geofiz.* **5** (4), 453–466.

ORSZAG, S. A. 1970 Analytical theories of turbulence. *J. Fluid Mech.* **41**, 363–386.

PANTON, R. L. 2001 Overview of the self-sustaining mechanisms of wall turbulence. *Prog. Aerosp. Sci.* **37** (4), 341–383.

PERRY, A. E. & CHONG, M. S. 1982 On the mechanism of wall turbulence. *J. Fluid Mech.* **119**, 173–217.

PERRY, A. E. & CHONG, M. S. 1994 Topology of flow patterns in vortex motions and turbulence. *Appl. Sci. Res.* **53** (3–4), 357–374.

PERRY, A. E., HENBEST, S. & CHONG, M. S. 1986 A theoretical and experimental study of wall turbulence. *J. Fluid Mech.* **165**, 163–199.

PIOMELLI, U., CABOT, W. H., MOIN, P. & LEE, S. 1991 Subgrid-scale backscatter in turbulent and transitional flows. *Phys. Fluids* **3** (7), 1766–1771.

PIROZZOLI, S. 2011 Flow organization near shear layers in turbulent wall-bounded flows. *J. Turbul.* **01**, N41.

RICHARDSON, L. F. 1920 The supply of energy from and to atmospheric eddies. *Proc. R. Soc. Lond.* A **97** (686), 354–373.

ROBINSON, S. K. 1991 Coherent motions in the turbulent boundary layer. *Annu. Rev. Fluid Mech.* **23** (1), 601–639.

ROGERS, M. M. & MOIN, P. 1987 The structure of the vorticity field in homogeneous turbulent flows. *J. Fluid Mech.* **176**, 33–66.

SADDOUGHI, S. G. & VEERAVALI, S. V. 1994 Local isotropy in turbulent boundary layers at high Reynolds numbers. *J. Fluid Mech.* **268**, 333–372.

SCHLATTER, P., LI, Q., ÖRLÜ, R., HUSSAIN, F. & HENNINGSON, D. 2014 On the near-wall vortical structures at moderate Reynolds numbers. *Eur. J. Mech. (*B*/Fluids)* **48**, 75–93.

SCHOPPA, W. & HUSSAIN, F. 2002 Coherent structure generation in near-wall turbulence. *J. Fluid Mech.* **453**, 57–108.

SINGER, B. A. & JOSLIN, R. D. 1994 Metamorphosis of a hairpin vortex into a Young turbulent spot. *Phys. Fluids* **6** (11), 3724–3736.

SUPONITSKY, V., AVITAL, E. & GASTER, M. 2005 On three-dimensionality and control of incompressible cavity flow. *Phys. Fluids* **17** (10), 104103.

SUTTON, M. A., WOLTERS, W. J., PETERS, W. H., RANSON, W. F. & MCNEILL, S. R. 1983 Determination of displacements using an improved digital correlation method. *Image Vis. Comput.* **1** (3), 133–139.

TANAHASHI, M., KANG, S., MIYAMOTO, T. & SHIOKAWA, S. 2004 Scaling law of fine scale eddies in turbulent channel flows up to $Re_\tau = 800$. *Intl J. Heat Fluid Flow* **25**, 331–341.

TAYLOR, G. I. 1938 The spectrum of turbulence. *Proc. R. Soc. Lond.* **164**, 476–490.

THEODORSEN, T. 1952 Mechanism of turbulence. In *Proceedings of 2nd Midwestern Conference of Fluid Mechanics*, Ohio State University.

TOMKINS, C. D. & ADRIAN, R. J. 2003 Spanwise structure and scale growth in turbulent boundary layers. *J. Fluid Mech.* **490**, 37–74.

TOWNSEND, A. A. 1961 Equilibrium layers and wall turbulence. *J. Fluid Mech.* **11**, 97–120.

TUERKE, F. & JIMÉNEZ, J. 2013 Simulations of turbulent channels with prescribed velocity profiles. *J. Fluid Mech.* **723**, 587–603.

VILLERMAUX, E., SIXOU, B. & GAGNE, Y. 1995 Intense vortical structures in grid-generated turbulence. *Phys. Fluids* **7** (8), 2008–2013.

WALLACE, J. M., ECKELMANN, H. & BRODKEY, R. S. 1972 The wall region in turbulent shear flow. *J. Fluid Mech.* **54**, 39–48.

WILLERT, C. E. & GHARIB, M. 1991 Digital particle image velocimetry. *Exp. Fluids* **10**, 181–193.

WILLMARTH, W. W. & LU, S. S. 1972 Structure of the Reynolds stress near the wall. *J. Fluid Mech.* **55**, 65–92.

WILLS, J. 1964 On convection velocities in turbulent shear flows. *J. Fluid Mech.* **20**, 417–432.

WU, X. & MOIN, P. 2010 Transitional and turbulent boundary layer with heat transfer. *Phys. Fluids* **22**, 085105.

ZHOU, J., ADRIAN, R. J., BALACHANDAR, S. & KENDALL, T. M. 1999 Mechanisms for generating coherent packets of hairpin vortices in channel flow. *J. Fluid Mech.* **387**, 353–396.